



Multimodal and spatially resolved profiling identifies distinct patterns of T cell infiltration in nodal B cell lymphoma entities

Received: 21 March 2023

Accepted: 15 January 2024

Published online: 20 February 2024

Check for updates

Tobias Roider 1,2,3,18, Marc A. Baertsch 1,4,18, Donnacha Fitzgerald 1,2,3, Harald Vöhringer 1,2,3, Berit J. Brinkmann 1,2,3,5, Felix Czernilofsky 1,2,3, Mareike Knoll³, Laura Llaó-Cid 6,7, Anna Mathioudaki 3, Bianca Faßbender⁸, Maxime Herbon⁸, Tobias Lautwein⁹, Peter-Martin Bruch 1,2,3,8, Nora Liebers^{3,8,10,11}, Christian M. Schürch 4,12, Verena Passerini¹³, Marc Seifert⁸, Alexander Brobeil¹⁴, Gunhild Mechtersheimer¹⁴, Carsten Müller-Tidow 1,2, Oliver Weigert 11,13,15, Martina Seiffert⁶, Garry P. Nolan 16, Wolfgang Huber 2,3,19 & Sascha Dietrich 1,2,3,8,17,19

The redirection of T cells has emerged as an attractive therapeutic principle in B cell non-Hodgkin lymphoma (B-NHL). However, a detailed characterization of lymphoma-infiltrating T cells across B-NHL entities is missing. Here we present an in-depth T cell reference map of nodal B-NHL, based on cellular indexing of transcriptomes and epitopes, T cell receptor sequencing, flow cytometry and multiplexed immunofluorescence applied to 101 lymph nodes from patients with diffuse large B cell, mantle cell, follicular or marginal zone lymphoma, and from healthy controls. This multimodal resource revealed quantitative and spatial aberrations of the T cell microenvironment across and within B-NHL entities. Quantitative differences in PD1⁺ TCF7⁺ cytotoxic T cells, T follicular helper cells or IKZF3⁺ regulatory T cells were linked to their clonal expansion. The abundance of PD1⁺ TCF7⁺ cytotoxic T cells was associated with poor survival. Our study portrays lymphoma-infiltrating T cells with unprecedented comprehensiveness and provides a unique resource for the investigation of lymphoma biology and prognosis.

Nodal B cell non-Hodgkin lymphomas (B-NHL) represent a heterogeneous group of indolent and aggressive malignancies. Extensive genetic and transcriptomic profiling has revealed mutational signatures and pathway dependencies, paving the way for molecular therapy^{1–8}. However, in recent years, T cell-engaging immunotherapies, such as bispecific antibodies or chimaeric antigen receptor T cells, have emerged among the leading treatment options for patients with refractory and relapsed B-NHL^{9–12}. Tailoring these treatment approaches to different B-NHL entities requires systematic investigation of the variety and functions of tumour-infiltrating T cells—analogously to studying the

genetic and transcriptomic makeup of tumour cells as a prerequisite for tailoring targeted therapies.

Traditionally, T cell phenotyping studies have been based on immunohistochemistry or flow cytometry¹³. In recent years, single-cell RNA sequencing (scRNA-seq) emerged as a powerful tool and became an integral part of T cell phenotyping efforts^{14,15}. We and others have pioneered the investigation of transcriptional heterogeneity of lymph node (LN)-derived T cells in B-NHL, but with the limitation of low sample sizes or having focused only on follicular lymphoma (FL, indolent)^{16–18}. Stand-alone scRNA-seq studies additionally face the

problem to align gene expression profiles with known T cell subsets that have been defined for decades based on surface epitopes and transcription factors¹⁹.

In this Resource, we employed cellular indexing of transcriptomes and epitopes by sequencing (CITE-seq), which simultaneously captures transcript and surface epitope abundances at single-cell resolution, and thus enables a multimodal identification of T cell phenotypes^{20,21}. Aiming to create a multimodal reference map of LN-derived T cells in nodal B-NHL, we collected more than 100 LN patient samples and included, besides FL, other B-NHL entities with only little or no prior groundwork: diffuse large B cell lymphoma (DLBCL, aggressive), marginal zone lymphoma (MZL, indolent) and mantle cell lymphoma (MCL, mixed). We identified and quantitated fine-grained T cell subsets and determined their clonality using full-length single-cell T cell receptor (scTCR) sequencing. We further assessed the ability of multicolour flow cytometry and multiplexed immunofluorescence to reproduce these T cell subsets and to localize them within the tumour microenvironment.

Results

Study and sample overview

We collected 101 LN samples (Extended Data Fig. 1a and Supplementary Table 1) from patients with DLBCL ($n = 28$), FL ($n = 30$), MZL ($n = 15$), MCL ($n = 15$), or from patients without evidence of malignancy (tumour-free/reactive LN (rLN), $n = 13$). LN samples from 38 patients were collected at initial diagnosis, while 50 LN samples were collected from patients who had received one or more prior lines of systemic treatment (Extended Data Fig. 1a). To minimize potential effects on T cell infiltration patterns, relapse samples were collected at least 3 months after cessation of the preceding treatment. T cell proportions of malignant LN samples determined by flow cytometry showed a broad variation (Extended Data Fig. 1a) but were not significantly associated with pre-treatment status, sex, age or B-NHL entity (Extended Data Fig. 1b–e).

Fourteen multimodally defined T cell subsets

We used CITE-seq to profile T cells from 51 LN patient samples. Surface proteins were detected using 70 oligonucleotide-tagged antibodies (Supplementary Table 2). After quality control and in silico sorting, we obtained data for 74,112 CD3⁺ T cells with a median of 1,190 T cells per patient sample. Unsupervised clustering based on a weighted combination of transcriptome and epitope similarities (weighted nearest neighbour)²² grouped the T cells into proliferating (T_{pr}), conventional helper (T_H) and follicular helper (T_{FH}), regulatory (T_{reg}), cytotoxic (T_{tox}) and double-negative T cells (T_{DN}, Fig. 1a). Differentially expressed genes and proteins (Fig. 1b,c) were associated with lineage (CD4 and CD8), functional specialization (for example, *FOXP3* and *ASCL2*), cytotoxicity (for example, *GZMA* and *GZMK*) or proliferation (for example, *MKI67*). These groups could be further partitioned into CD4⁺ and CD8⁺ naive T cells, central memory (CM₁ and CM₂) T_H cells, central memory (CM₁ and CM₂) and effector memory (EM₁ and EM₂) T_{reg} cells, and effector memory (EM₁, EM₂ and EM₃) T_{tox} cells. At this level of granularity, differentially expressed markers (Fig. 1b,c) were linked to differentiation (for example, CD45RA, CD45RO and CD62L), homing and migration (for example, *KLF2* and *CCR7*), activation (for example, CD69, CD38 and CD278) and inhibition (for example, PD1, TIM3 and LAG3). This high-granularity classification was supported by a gene regulatory network analysis²³, which highlighted differential activities of specific transcription factors (for example, *KLF2* (ref. 24), *TCF7* (ref. 25), *FOXP3* (ref. 26) and *ASCL2* (ref. 27), Fig. 1d). On this basis, we compiled profiles of the most discriminating and biologically interpretable surface proteins, genes and transcription factors (Fig. 1e). Further extended profiles are provided in Supplementary Table 3.

Cytometry reproduces multimodally defined T cell subsets

Next, we built gradient boosting classifiers²⁸ to identify the most discriminatory surface markers between multimodally defined subsets

(Fig. 2a). While this yielded accurate results for most T cell subsets (Extended Data Fig. 2a), the distinction among T_{reg} cells and the detection of T_{pr} cells could be improved by additional intracellular markers (Ki67, FOXP3 and IKZF3; Extended Data Fig. 2b). After removal of redundant (for example, CD95 and CD127) and less important markers, we thus compiled a 12- and 13-plex flow cytometry panel (Supplementary Table 4) and established gating strategies supported by the hypergate algorithm²⁹, which enabled classification of all 14 multimodally defined T cell subsets (Supplementary Figs. 1 and 2). We correlated the subset proportions determined by CITE-seq and flow cytometry in a total of 13 LN samples and observed a median Pearson coefficient of 0.92 across all subsets (Fig. 2b). We then applied these panels to an independent cohort of 50 LN samples, which was then used for further quantitative analysis of T cell infiltration patterns.

Quantitative patterns of T cell infiltration in nodal B-NHL

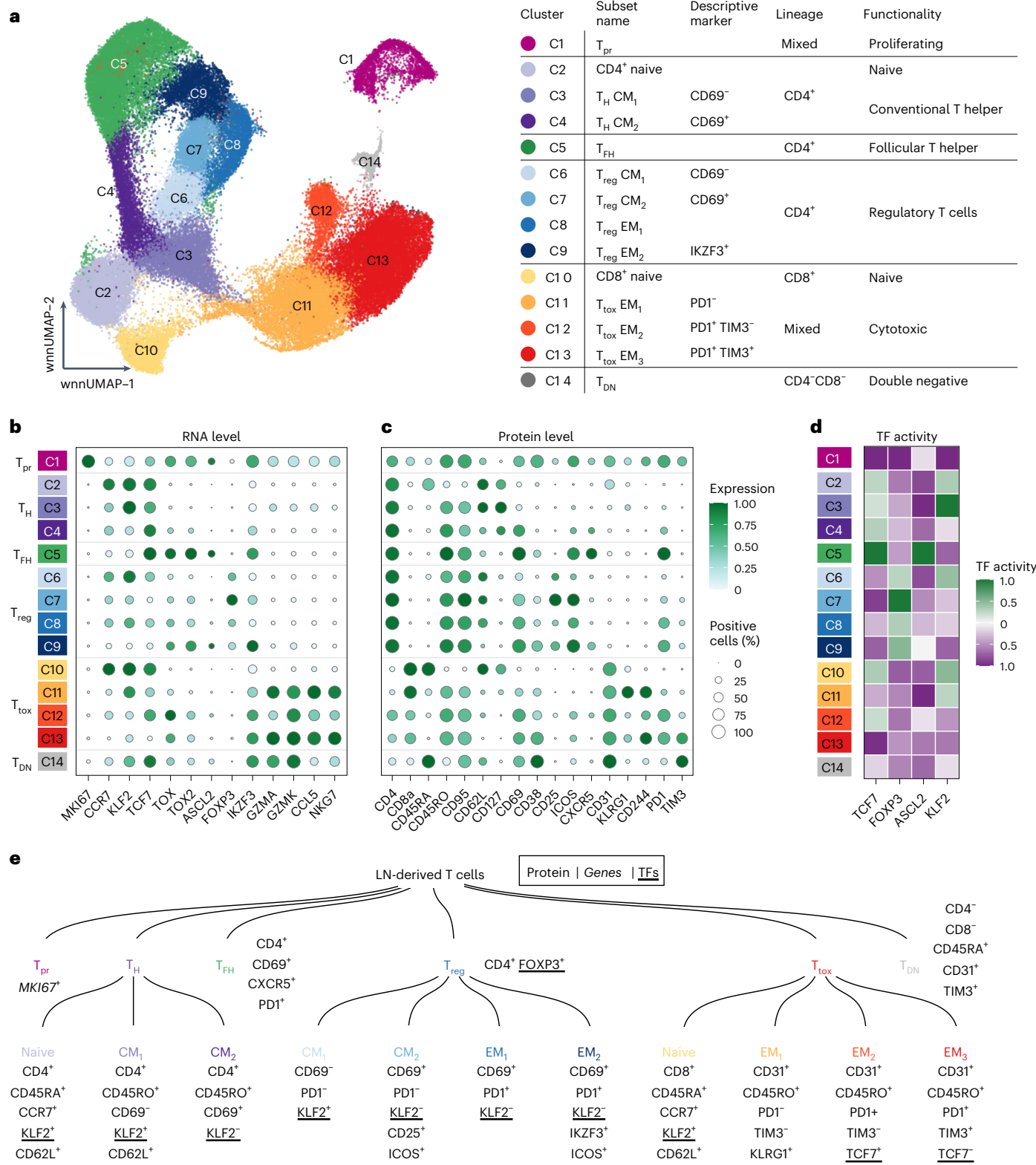
We combined CITE-seq and flow cytometry data, determined the proportion of each subset per sample, and compared each B-NHL entity with tumour-free LN samples (Fig. 3a). B-NHL were characterized by a lack of CD69⁺ CM₁ and CD69⁺ CM₂ T_H cells, and CD4⁺/CD8⁺ naive T cells (Fig. 3a). Conversely, PD1⁺ TIM3[−] T_{tox} EM₂ cells and PD1⁺ TIM3⁺ EM₃ T_{tox} cells, T_{pr} cells and CD69⁺ T_{reg} CM₂ cells were significantly enriched in B-NHL (Fig. 3a). FL and MZL were additionally characterized by significant enrichment of T_{FH} and IKZF3⁺ T_{reg} EM₂ cells (Fig. 3a). We also noted a significant increase of CD69⁺ T_{reg} CM₂ cells in MCL, FL and MZL, whereas T_{FH} cells were depleted in DLBCL (Fig. 3a). We observed similar results when using (absolute) subset frequencies instead of (relative) subset proportions (Extended Data Fig. 3). To gain a broader overview of these differences across all B-NHL entities, we used principal component analysis (PCA) on the table of subset proportions and the overall T cell frequency (Fig. 3b). Based on the first two principal components (PCs), we identified three major groups (I–III) represented by tumour-free (I), DLBCL and MCL (II), and FL and MZL LNs (III, Fig. 3b). PC1 (Fig. 3c) and PC2 (Fig. 3d) had high loadings on the characteristic T cell subsets highlighted in Fig. 3a: CD4⁺ and CD8⁺ naive T cells, and PD1⁺ TIM3⁺ T_{tox} EM₃ cells (PC1), and T_{FH} and IKZF3⁺ T_{reg} EM₂ cells (PC2).

To further explore to what extent T cell composition and frequency is distinctive for different B-NHL entities and tumour-free LN, we built classifiers using LASSO-regularized multinomial logistic regression and estimated classification accuracy using nested leave-one-out cross-validation (Fig. 3e and Extended Data Fig. 4a). Accuracy was best for distinguishing between tumour-free and malignant LNs (balanced accuracy of 74.5%); moreover, DLBCL and MCL could be differentiated with similar accuracy (Fig. 3e). A third, well-distinguishable group was formed by FL and MZL (Fig. 3e). These results indicate that different entities have distinct patterns of T cell infiltration (Extended Data Fig. 4a), although—based on our current data—classification does not provide diagnostic accuracy.

To explore the potential role of patient-inherent characteristics, we fit multivariate linear models using sex, age, treatment status and cell-of-origin (only DLBCL) as covariates, and the proportion of each T cell subset as dependent variable (Extended Data Fig. 4b). We found that pre-treatment (Fig. 3f, $P < 0.001$) and higher age (Fig. 3g, $P = 0.04$) were associated with a lower proportion of naive CD4⁺ T cells. Pre-treatment was also linked to a lower proportion of CD69⁺ T_H CM₂ cells (Fig. 3h, $P < 0.001$) and a higher proportion of CD69⁺ T_{reg} CM₂ cells (Fig. 3i, $P < 0.001$), while we observed no statistically significant effect on the T cell composition for sex and cell-of-origin (Extended Data Fig. 4b). Larger sample sizes might be necessary to detect less strong associations, but overall, patient characteristics had only a moderate effect on the T cell composition compared with entity-specific differences.

Entity-specific clonality of CD4⁺ and CD8⁺ T cell subsets

To investigate whether the enrichment of T cell subsets results from their clonal expansion, we performed full-length scTCR sequencing

**Fig. 1 | LN-derived T cells can be divided into 14 multimodally defined subsets.**

a, CITE-seq data from 51 primary LN patient samples were integrated and jointly visualized using UMAP. Cells were coloured with respect to their cluster on the basis of a shared nearest neighbour-based algorithm. The adjacent table summarizes all clusters including used subset names, lineages and functionality.

b,c, Dot plot showing the expression of important marker genes and proteins to identify all T cell subsets. Size and colour of the dots indicate the percentage

of positive cells and scaled gene/protein expression, respectively. Values were scaled between 0 and 1. **d**, Heatmap showing the inferred activity of selected transcription factors (TFs), as indicated. *y* axis is identical to **b** and **c**. Values were scaled between -1 and 1. **e**, Dendrogram summarizing the 14 multimodally defined T cell subsets including most important and interpretable marker genes, proteins and transcription factors.

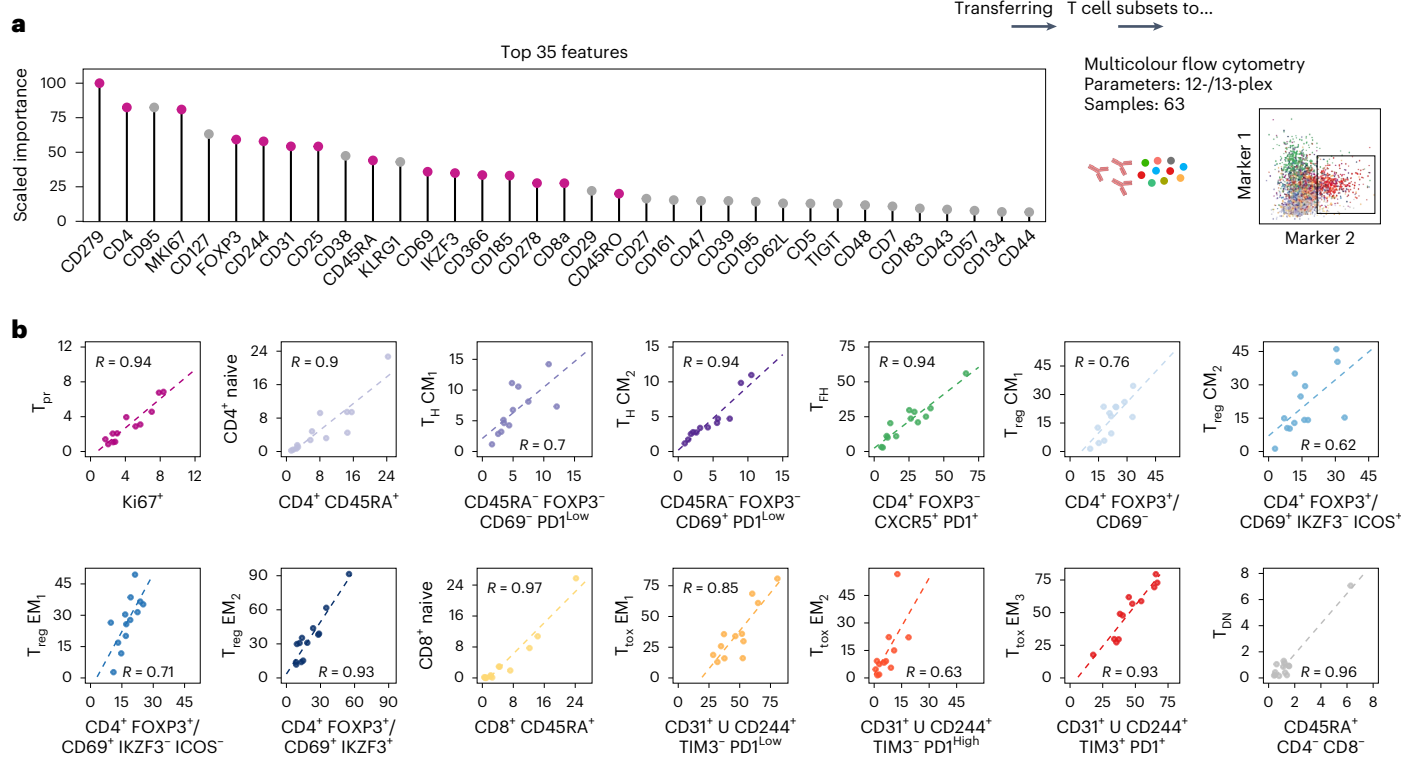


Fig. 2 | Multicolour flow cytometry reproduces multimodally defined T cell subsets. **a**, Most important features to distinguish multimodally defined T cell subsets using a gradient boosting classifier. Only features that are routinely accessible by flow cytometry were considered for the model. **b**, Percentages of

all T cell subsets determined by flow cytometry (x axis) and CITE-seq (y axis) were correlated for $n = 13$ biologically independent samples. x axis title indicates the applied gating strategy. The symbol 'U' indicates merging of two populations. Pearson's correlation coefficient is given for each panel (R).

alongside 5' scRNA-seq in a representative subset of 17 patient samples (Extended Data Fig. 1a and Supplementary Table 1). After quality control, 5' scRNA and full-length TCR data were available for 66,896 T cells with a median of 3,045 cells per patient sample. We mapped the 5' scRNA onto the CITE-seq reference data above, indicating high consistency of the inferred subset proportions between both modalities with a median correlation coefficient of $R = 0.92$ (Extended Data Fig. 5a). Then, we compiled the scTCR data to clonotypes on the basis of their complementarity-determining regions³⁰ and projected them onto the reference uniform manifold approximation and projection (UMAP; Fig. 4a). Clonally expanded T_{tox} EM₁ cells were present across all entities and in tumour-free LNs (Fig. 4a), while clonally expanded PD1⁺ TIM3⁺ T_{tox} EM₃ cells were limited to DLBCL, FL and MZL (Fig. 4a). Clonality of T_{tox} cells was not restricted to CD8⁺ but included also CD4⁺ T_{tox} cells (Extended Data Fig. 5b,c). In addition, T_{FH} and IKZF3⁺ T_{reg} EM₂ cells were clonally expanded exclusively in FL and MZL (Fig. 4a). Consequently, the TCR diversity was substantially reduced in DLBCL, FL and MZL samples compared with tumour-free and MCL samples (Extended Data Fig. 5d–f). To further support our findings, we quantified the proportion of clonally expanded T cells per subset and compared each entity with tumour-free samples. While T_{tox} EM₁ cells were clonally expanded to a similar extent across all sample types, T_{tox} EM₃ cells, T_{FH} cells and T_{reg} EM₂ cells had significantly enriched proportions of clonally expanded T cells only in entities specified above (Fig. 4b). We further used scTCR data to track the original identity of T_{pr} cells, that is at the time of sample collection temporarily masked by an S or G₂M phase-dependent gene expression signature³¹. Apart from MCL and tumour-free LN, which both harboured very low proportions of T_{pr} cells (Fig. 4a,c), we identified groups of shared clonotypes in DLBCL, FL and MZL predominantly between T_{pr} cells and PD1⁺ TIM3⁺ T_{tox} EM₃ cells (Fig. 4c). To a lower extent, TCR clonotypes were also shared

between T_{pr} cells and T_{FH} cells, and between T_{pr} cells and IKZF3⁺ T_{reg} EM₂ cells in FL and MZL (Fig. 4c). Overall, this analysis highlights that an altered T cell microenvironment results from active proliferation and differential expansion of specific T cell subsets.

PD1⁺ TCF7⁺ T_{tox} cells converge into exhausted T cells

To unveil the process of T cell exhaustion across B-NHL entities in detail, we performed a trajectory analysis³² of T_{tox} cells based on the CITE-seq data. We identified two paths: (I) one from naive to PD1⁺ TIM3⁺ T_{tox} EM₂ cells, and (II) another one from naive to PD1⁺ TIM3⁺ T_{tox} EM₃ cells (Fig. 5a). Apart from TIM3, both expression (Fig. 5b) and inferred transcription factor activity²³ of *TCF7* was an important discriminator between both trajectories (Fig. 1d). *TCF1* (encoded by *TCF7*) is a hallmark of stemness and longevity and its presence (trajectory I) or absence (trajectory II) indicates maintained or impaired self-renewal capacity, respectively³³, thereby suggesting that only trajectory II converges into terminally exhausted T cells.

To further resolve gradual changes along trajectory II, we applied pseudotime analysis³² and ranked the cells starting from naive T_{tox} cells (Fig. 5a). We found that pseudotime was strongly linked to a continuously increasing expression of both differentiation and activation markers, such as CD45RO, CD69, CD38 and ICOS, and inhibitory molecules, such as PD1, TIM3, LAG3, TIGIT and CD39 (Fig. 5c). Cells with the highest levels of inhibitory receptors had reduced RNA expression levels of effector molecules, particularly of *GZMA* and *GZMH*, and reduced protein levels of CD244 (ref. 34) (Fig. 5c). Likewise, the inferred activity²³ of the transcription factors PRDM1, BATF, IRF4 and EOMES, which have previously been associated with T cell exhaustion^{35–38}, were strongest in T_{tox} cells at the end of the trajectory (highest pseudotime), whereas the inferred transcription factor activity of *TCF7* was lowest in these cells (Fig. 5c). On this basis, we established a signature profile

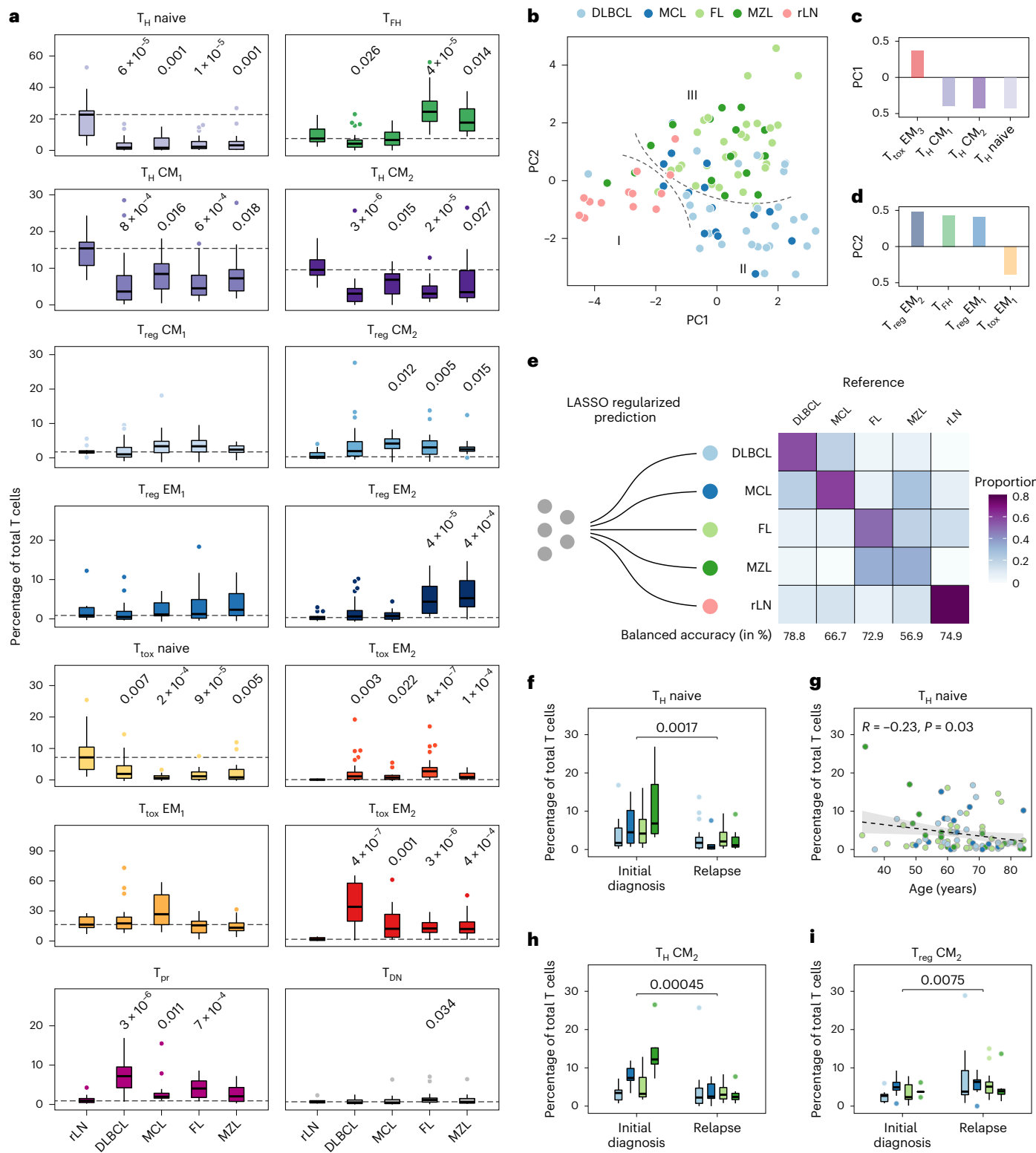


Fig. 3 | Nodal B-NHL entities have characteristic quantitative patterns of T cell infiltration. **a**, T cell subset proportions determined by CITE-seq or flow cytometry are illustrated in box plots ($n=101$ biologically independent patient samples). Outliers are shown as individual dots. Each entity and subset were tested versus tumour-free samples (rLN) using a two-sided Wilcoxon test. P values were corrected for multiple testing using the Benjamini–Hochberg procedure. Only P values ≤ 0.05 are shown. Dashed lines indicate the median of rLN. **b–d**, PCA based on the subset and overall T cell proportions (**b**) including the top four loadings of PC1 (**c**) and PC2 (**d**) are shown. Dashed lines (**b**) highlight three groups (I–III) of samples. **e**, Confusion matrix based on a

LASSO-regularized multinomial logistic regression model and estimated classification accuracy using leaving-one-out cross-validation based on subset and overall T cell proportions. **f–i**, Patient characteristics were evaluated in a multivariate model regarding their effect on the proportions of all 14 T cell subsets. Shown are the four most significant associations. P values and/or correlation coefficients were calculated using a two-sided Wilcoxon test (**f**, **h** and **i**) or Pearson's linear correlation (**g**). Box plots or dots are coloured by entity as in **b** and **e**. The error band in **g** indicates the 95% confidence interval. Box plots: centre line, median; box limits, first and third quartile; whiskers, $1.5 \times$ interquartile range.

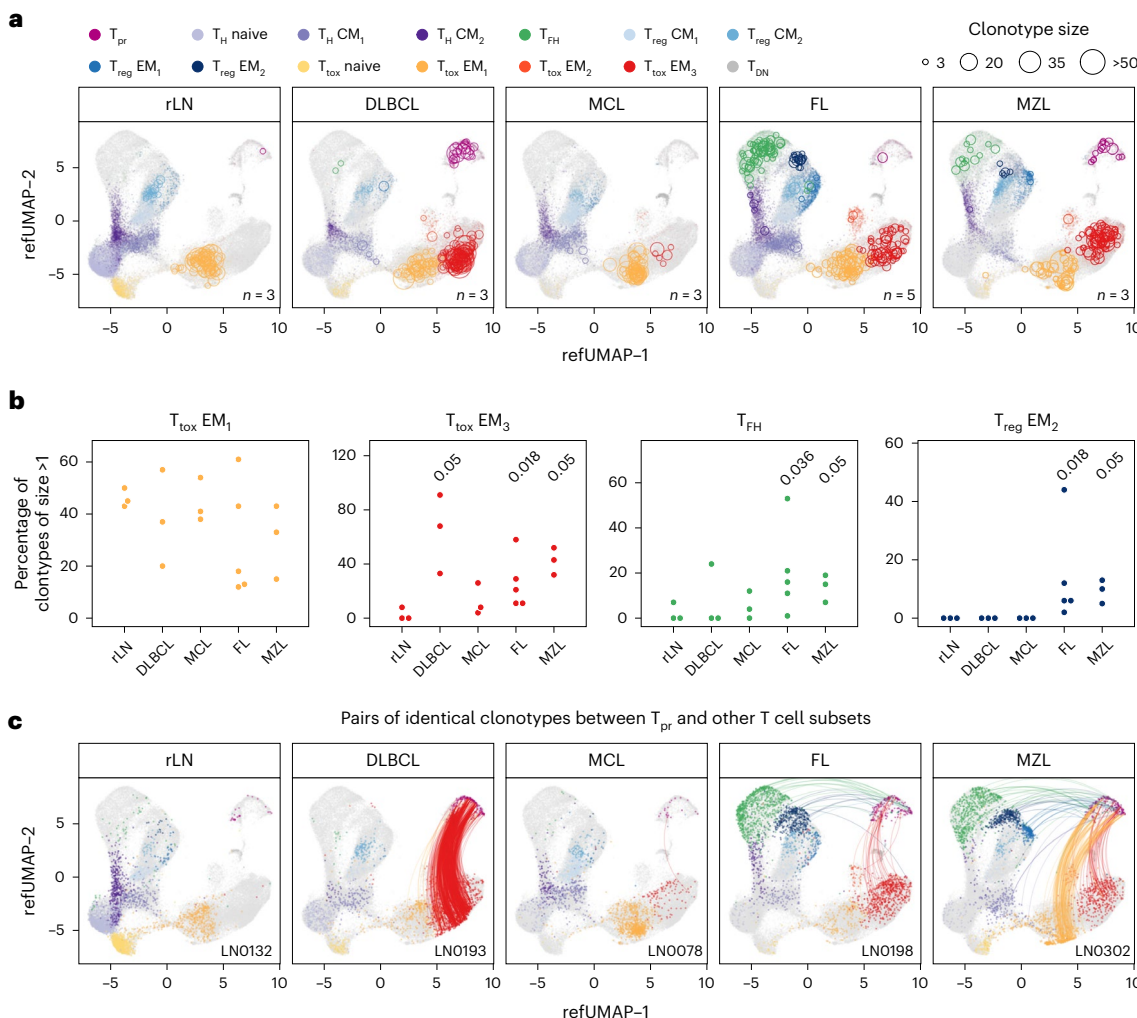


Fig. 4 | Entity-specific T cell compositions result from differential clonal expansion of CD4⁺ and CD8⁺ T cell subsets. **a, b**, 5' scRNA alongside full-length TCR repertoire data were mapped to the CITE-seq reference dataset. In grey, all cells with 5' scRNA data are shown, whereas coloured cells belong to samples derived from specific entities (a) or samples (b), as indicated. The number of biologically independent samples is indicated in each panel. In a, circles represent the number of cells with identical TCR clonotype within the same

subpopulation. To avoid overplotting, a maximum of 30 circles per sample and T cell subset is shown. In b, the percentage of clonally expanded T cells per patient and T cell subset, as indicated, was quantified and compared with tumour-free samples. Each entity and subset were tested versus tumour-free samples (rLN) using a one-sided Wilcoxon test. Only *P* values ≤ 0.05 are shown. **c**, Mapped cells from five representative samples. Lines connect all proliferating cells with any other cell given that both have identical TCR clonotypes.

(Supplementary Table 5), to facilitate the identification of terminally exhausted T cells in scRNA-seq data (Extended Data Fig. 6a). While the initial trajectory and pseudotime analysis was performed on complete T_{tox} cells, scoring gave similarly high values when applied separately to CD4⁺ or CD8⁺ T_{tox} cells (Extended Data Fig. 6b).

Plotting the proportion of T_{tox} cells by sample and pseudotime revealed that terminally exhausted T cells were most abundant in DLBCL and FL, most variable in MZL, and lowest in MCL (Fig. 5d). Clonality analysis based on scTCR data supported this finding by demonstrating that the expansion of PD1⁺ TIM3⁺ T_{tox} EM₃ cells was a key feature of the tumour microenvironment of DLBCL, FL and MZL, while MCL and tumour-free LNs were predominantly characterized by clonal PD1⁺ T_{tox} EM₁ cells (Fig. 4a).

T cell exhaustion is linked to adverse prognosis in B-NHL

To investigate if T cell exhaustion is associated with clinical outcome in B-NHL, we extracted a transcriptional signature from terminally exhausted T cells of our data and applied digital cytometry³⁹ to bulk RNA data from two large independent retrospective DLBCL cohorts^{2,4}.

We found that a higher proportion of terminally exhausted T_{tox} cells was associated with inferior progression-free survival in both cohorts (Fig. 5e, *P* = 0.003, Fig. 5f, *P* = 0.011). Moreover, the cohort from Schmitz et al.⁴ harboured higher proportions of exhausted T cells in ABC- than GCB-subtype DLBCL (Extended Data Fig. 6c), which is in line with a recent flow cytometry-based study⁴⁰. However, there was no difference between ABC- and GCB-subtype DLBCL in our data (Extended Data Fig. 4b) or in the cohort from Chapuy et al.² (Extended Data Fig. 6d). Neither of the genetic subtypes defined in these cohorts were associated with the proportion of exhausted T_{tox} cells (Extended Data Fig. 6c,d). We also evaluated individual somatic mutations (for example, *MYD88*), amplifications (for example, *BCL2*), deletions (for example, 17p) and structural variants (for example, *BCL6*). After correction for multiple testing, none of the genetic aberrations was associated with the proportion of exhausted T_{tox} cells (Extended Data Fig. 6e-h). We performed a similar analysis using bulk RNA-seq data of a prospective FL cohort of the GALLIUM trial (NCT01332968)^{41,42}, and again a higher proportion of exhausted T cells was associated with inferior survival (Fig. 5g, *P* = 0.04).

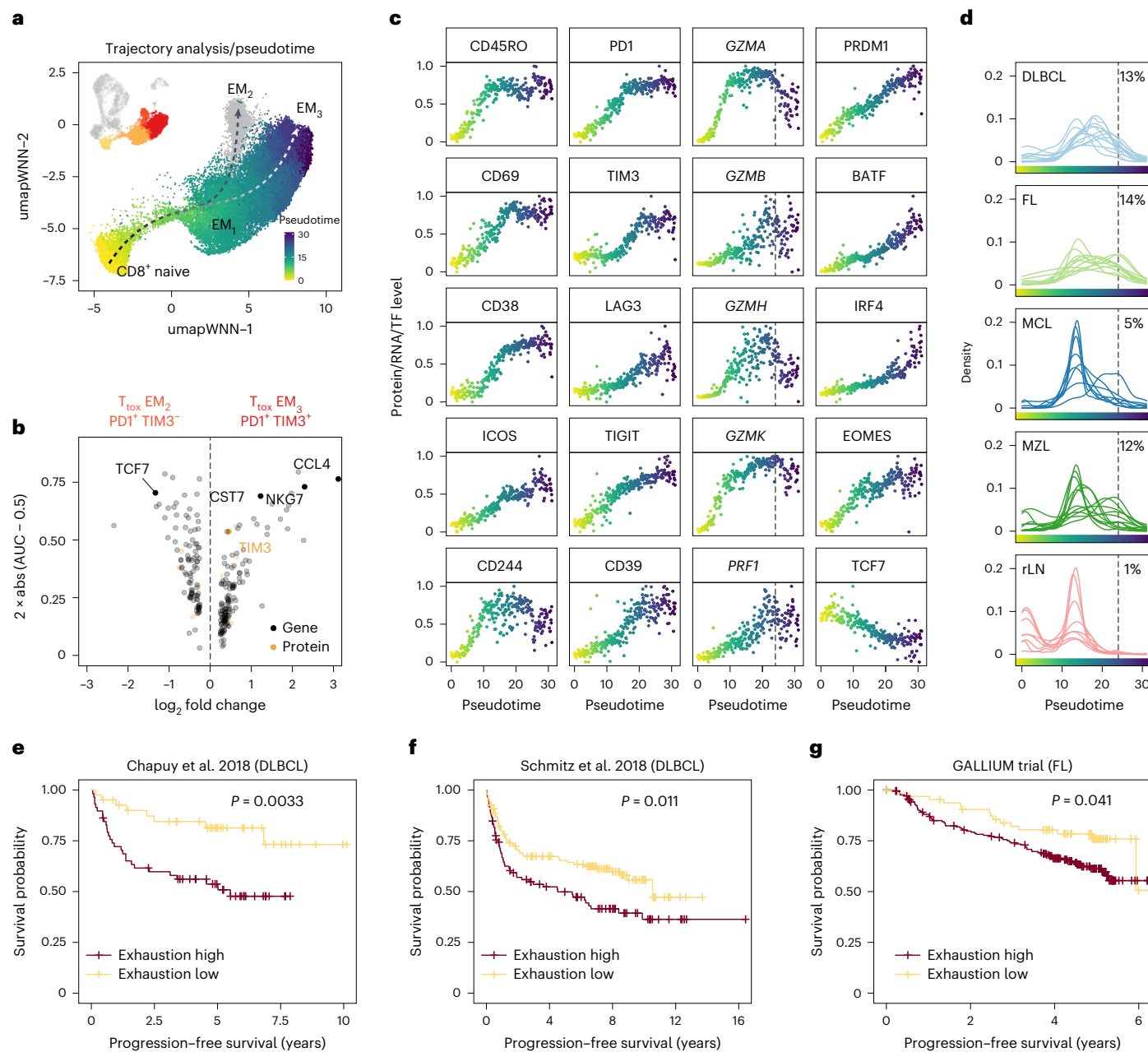


Fig. 5 | PD1⁺ TCF7⁻ cytotoxic T cells converge into terminally exhausted T cells with variable proportions within and across entities. **a**, Combined trajectory and pseudotime analysis were performed using CITE-seq expression profiles of T_{tox} cells starting from naive CD8⁺ T cells. Arrows illustrate trajectories, while cells are coloured by pseudotime. **b**, Volcano plot illustrating differentially expressed genes and proteins between PDI⁺ TIM3⁺ T_{tox} EM₃ cells and PDI⁺ TIM3⁺ T_{tox} EM₂ cells. **c**, Protein expression (first and second column), gene expression (third column) or inferred transcription factor activity (fourth column) are illustrated along

binned pseudotime, as shown in **a**. Values were scaled between 0 and 1. Dashed lines indicate threshold when T cells were considered terminally exhausted.

d, Shown is the density of cells for each single patient along pseudotime. Number indicates median percentage of terminally exhausted T cells across all LN patient samples for each entity. **e–g**, Bulk RNA-seq data from patients with DLBCL (**e** and **f**) and FL (**g**) were deconvoluted on the basis of a gene expression signature of terminally exhausted T cells. Kaplan–Meier plots with *P* values of corresponding log-rank test. AUC, area under the curve.

IKZF3⁺ T_{reg} EM₂ cells are clonally related to T_{FH} cells

In FL and MZL, not only T_{tox} cells but also T_{FH} and T_{reg} EM₂ cells were clonally expanded (Fig. 4a) and significantly enriched (Fig. 6a). While T_{FH} cells are well characterized and known to promote the growth of malignant B cells in FL⁴³, the role of LN-derived T_{reg} cells in nodal B-NHL has not been investigated systematically. Aiming to characterize T_{reg} EM₂ cells, we compared protein and gene expression profiles of T_{reg} EM₂ cells and T_{reg} EM₁ cells, and found that T_{reg} EM₂ cells were characterized by high protein levels of CD69, ICOS, CD38, PD1 and TIGIT (Fig. 6b). At the

gene expression level, T_{reg} EM₂ cells showed high expression of *IKZF3*, *CXCL13* and *ASCL2*, but low expression of *KLF2* and *IKZF2* (Fig. 6c). We used flow cytometry to confirm the presence of IKZF3 on protein level (Extended Data Fig. 7a) and the enrichment of IKZF3⁺ T_{reg} cells in MZL and FL using an independent cohort of 24 LN samples (Extended Data Fig. 7b). IKZF2, alias Helios, is well studied as a marker of natural T_{reg} cells⁴⁴, but only few studies have explored the role of IKZF3, alias Aiolos, in T_{reg} cells. A previous study suggested that IKZF3⁺ T_{reg} cells usually lack IKZF2 and represent an inducible rather than natural T_{reg} cell subset with

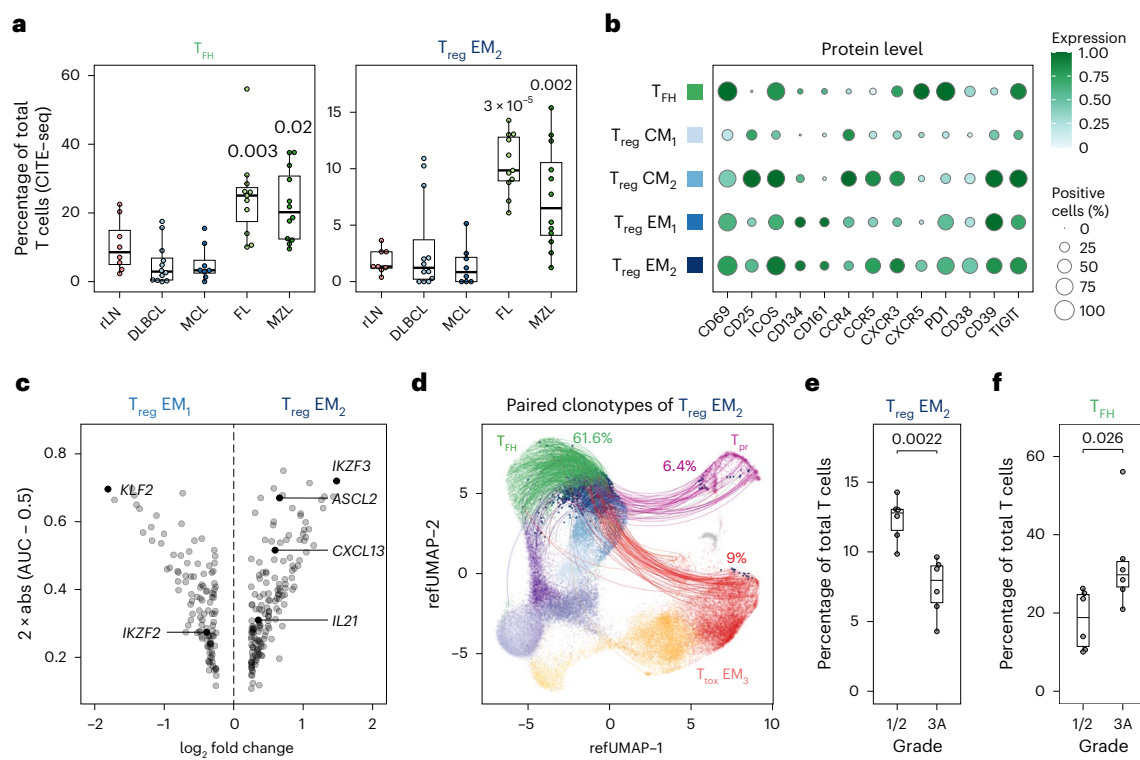


Fig. 6 | IKZF3⁺ T_{reg} EM₂ cells are clonally related to T_{fh} cells and associated with grading of FL. **a**, Proportions of T_{reg} EM₂ cells and T_{fh} cells determined by CITE-seq are illustrated as box plots ($n = 51$ biologically independent patient samples). All entities were tested for significance using a two-sided Wilcoxon test with rLN as reference. Only P values ≤ 0.05 are shown. **b**, Dot plot showing the expression of important phenotypic proteins. Size and colour of the dots indicate the percentage of positive cells and scaled protein expression, respectively. Values were scaled between 0 and 1. **c**, Volcano plot illustrating differentially expressed genes between T_{reg} EM₂ cells and EM₁ cells. **d**, 5' scRNA alongside full-length TCR

repertoire data were mapped to the CITE-seq reference data. Lines connect all T_{reg} EM₂ cells with any other cell given that both T cells have the same TCR clonotype. Percentages indicate shares of overlapping clonotypes for T_{fh} cells, T_{pr} cells and T_{tox} cells. Analysis is based on $n = 17$ biologically independent patient samples. **e,f**, Proportions of T_{reg} EM₂ cells (**e**) and T_{fh} cells (**f**) determined by CITE-seq are shown in dependence of tumour grading in FL (1/2 versus 3A). Differences were tested for significance using a two-sided Wilcoxon test. Shown are $n = 12$ biologically independent patient samples. Box plots: centre line, median; box limits, first and third quartile; whiskers, 1.5 \times interquartile range.

potent suppressive capacity⁴⁵. On this basis, we intended to identify potential populations related to T_{reg} EM₂ cells using scTCR data. We found that T_{reg} EM₂ cells share a substantial proportion of clonotypes with T_{fh} cells (Fig. 6d), whereas this was not the case for other T_{reg} cell populations (Extended Data Fig. 7c). Based on these aspects, IKZF3⁺ T_{reg} cells could resemble follicular regulatory T cells⁴⁶.

We further investigated whether the proportion of T_{reg} EM₂ cells was associated with clinical parameters. Lower-grade (1/2) FL had a higher proportion of T_{reg} EM₂ cells (Fig. 6e, $P = 0.002$), whereas higher-grade FL (3A) had a higher proportion of T_{fh} cells (Fig. 6f, $P = 0.03$). We applied digital cytometry³⁹ on the GALLIUM cohort^{41,42} to estimate the proportion of T_{reg} EM₂ cells and T_{fh} cells, and to investigate whether these subsets were associated with progression-free survival. Indeed, there was a trend towards inferior prognosis in patients with higher proportions of T_{fh} cells ($P = 0.05$, Extended Data Fig. 7d), while no association was found for T_{reg} EM₂ cells ($P = 0.17$, Extended Data Fig. 7e).

CODEX captures the tumour and T cell microenvironment

To localize T cell subsets in their spatial context, we used highly multiplexed immunofluorescence in formalin-fixed paraffin-embedded (FFPE) LN tissues using co-detection by indexing (CODEX)⁴⁷. We established a panel of 50 antibodies (Supplementary Table 6) and imaged 35 FFPE biopsy cores from 19 patient samples (Extended Data Fig. 1a and Supplementary Table 1). Finally, we identified B cells, T cells, natural killer (NK) cells, NKT cells, mast cells, plasma cells, dendritic cells, follicular dendritic cells (FDCs) and stromal cells, as well as macrophages and granulocytes (Extended Data Fig. 8a-c). Among a total of around

5.5 million processed cells, we detected a median of approximately 45,000 T cells per tissue core (Extended Data Fig. 8d), which we further divided into eight subpopulations including naive CD4⁺ and CD8⁺ T cells (CD45RA⁺), T_{fh} cells (CD45RO⁺, PDI⁺, CXCR5⁺), T_{reg} cells (FOXP3⁺), memory CD4⁺ cells (CD45RO⁺), memory CD8⁺ T_{tox} cells (CD45RO⁺), exhausted T_{tox} cells (CD45RO⁺, PDI⁺, TIM3⁺) and T_{pr} cells (Ki67⁺, Extended Data Fig. 8a,c). A high-granularity classification of T cell subsets, as possible with the CITE-seq and flow cytometry, was hampered by lower signal-to-noise ratio (for example, CD62L and CD69) or reduced sensitivity of available antibodies (for example, IKZF3). Still, we aligned the low-granularity T cell subpopulations detected by multiplexed immunofluorescence with the 14 high-granularity T cell subsets identified by CITE-seq (Extended Data Fig. 8a), resulting in a median Pearson coefficient of 0.71 across all subpopulations (Extended Data Fig. 8e).

B-NHL generates entity-specific microenvironmental patterns

In situ mapping of the above-mentioned cell types and T cell subpopulations enabled an intuitive visualization of tumour-free or malignant LN structure (Fig. 7a and Extended Data Fig. 9). To capture spatial organization systematically, we identified the 25 nearest neighbours of each cell by a sliding window approach and tabulated the frequencies of cell types and T cell subsets in each window. We used k-means clustering on the neighbour frequency tables to identify ten recurrent neighbourhoods (N1–N10; Fig. 7b) and PCA to identify the cell types most important for distinguishing N1 to N10 (Fig. 7c). Seven out of ten neighbourhoods captured important elements of intact LN architecture, including B cell follicles (N1) with T_{fh}-rich and FDC-rich germinal

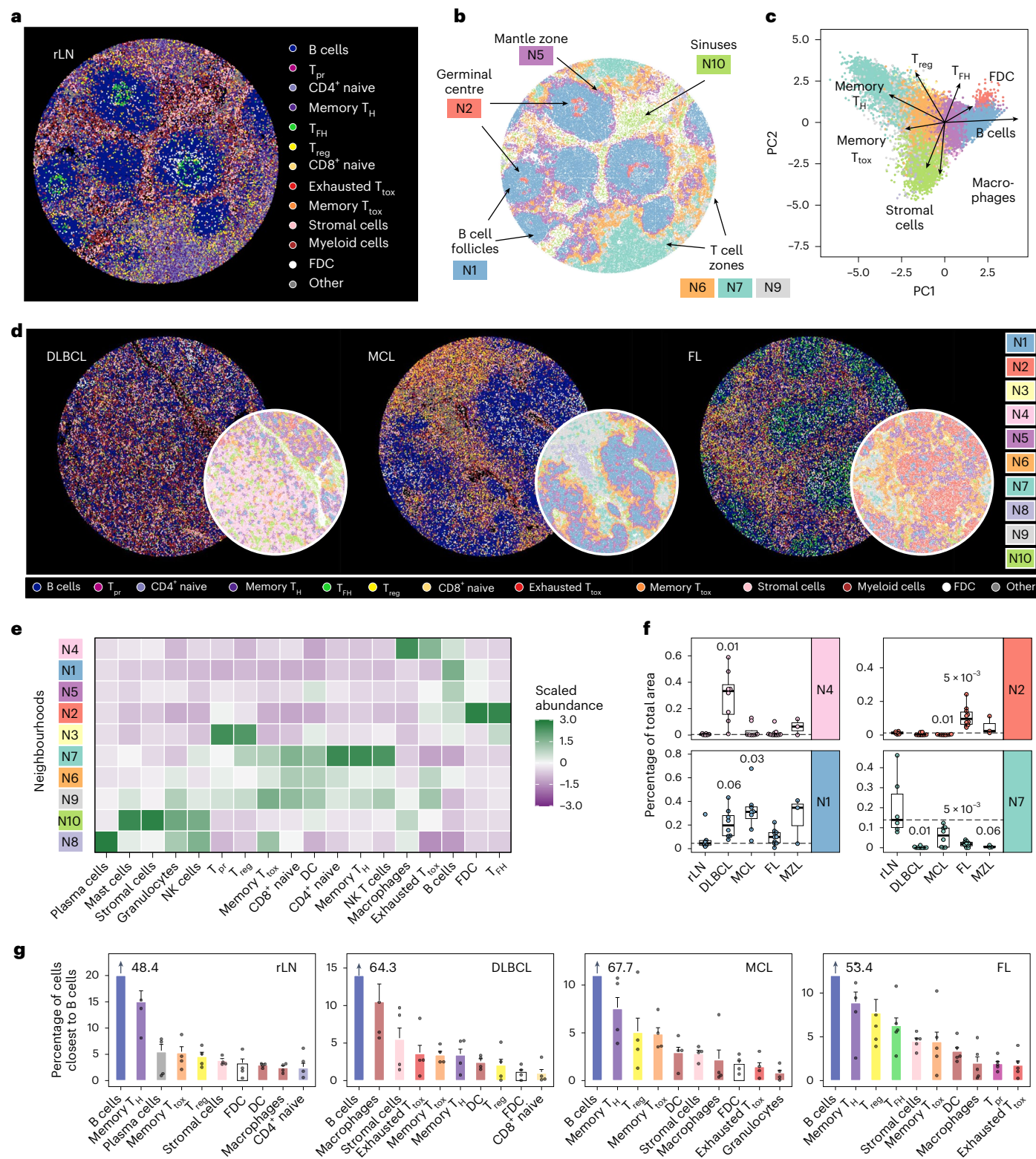


Fig. 7 | B-NHL disrupts the healthy LN architecture and generates entity-specific microenvironmental patterns. a, b. Each cell of a representative tumour-free LN-derived tissue core (rLN) is coloured by its subpopulation (a) or neighbourhood (b). **c.** Neighbourhoods shown in b were subjected to PCA. The top four loadings of components 1 and 2 are shown as vectors. **d.** Representative LN-derived tissue cores infiltrated by DLBCL, MCL or FL. Each cell is coloured by subpopulation or neighbourhood. **e.** Heatmap illustrating the mean and column-wise scaled abundance of subpopulations per neighbourhood across the complete mIF dataset. **f.** Box plots showing the proportions of selected

neighbourhoods of each tissue core. Each entity and neighbourhood were tested versus rLN using the two-sided Wilcoxon test. P values were corrected for multiple testing using the Benjamini–Hochberg procedure. Only P values ≤ 0.05 are shown. Dashed lines indicate the median of tumour-free LNs (rLN).

g. Bar plots showing percentages of cells that were located closest to B cells. DC, dendritic cells. Error bars represent s.e.m. For illustration purposes the B cell bar is not shown completely but indicated as number. In e–g, $N=19$ biologically independent samples are shown.

centres (N2), follicle-surrounding mantle zones (N5), inter-follicular T cell zones (N6, N7 and N9) and sinuses (N10) harbouring predominantly stromal cells, macrophages, mast cells, granulocytes and NK cells (Fig. 7a–c), whereas N3, N4 and N8 could not be assigned to physiological LN regions.

The described pattern was preserved in all tumour-free tissue cores (Extended Data Fig. 10a) but largely disrupted in B-NHL LNs (Fig. 7d and Extended Data Fig. 10b–e). LN-derived tissue cores infiltrated by DLBCL had the least degree of structure and exhibited a diffuse excess of a neighbourhood (N4) harbouring exhausted T cells, macrophages and tumour cells, whereas neighbourhoods (N7 and N8) rich in naïve and memory T_H cells and T_{tox} cells were absent (Fig. 7d–f and Extended Data Fig. 10b). Tissue cores from LNs infiltrated by FL were characterized by expansion of germinal centre-like areas (N2) containing high numbers of (clonal) T_{FH} cells and FDC, surrounded by areas (N6 and N9) containing T_{reg} memory T_H cells, and memory and exhausted T_{tox} cells, but also B cells (Fig. 7d–f and Extended Data Fig. 10d). In tissue cores infiltrated by MCL, we found a significant predominance of follicle-like B cell areas (N1, Fig. 7f), where T_{FH} cells and germinal centres were absent (Fig. 7d,e and Extended Data Fig. 10c). In contrast to DLBCL and FL, B cell areas in MCL were well separated and barely infiltrated by T cells (Fig. 7d and Extended Data Fig. 9), resulting in only little contact surface in the transition areas (N6, Fig. 7d,e). To identify interaction partners of B cells on the basis of spatial proximity, we determined the nearest neighbour of each B cell and ranked them by frequency (Fig. 7g). This analysis suggested strikingly different interaction partner across entities: While B cells derived from FL, MCL and tumour-free LNs were in closest contact to varying T cell subsets, for instance T_{reg} cells and T_{FH} cells in FL, we observed that B cells derived from DLBCL were mostly surrounded by macrophages and stromal and exhausted T cells (Fig. 7g).

Discussion

Our study provides an in-depth and systematic reference map of LN-derived T cells in DLBCL, FL, MCL, MZL and tumour-free samples. Across all entities, malignant LNs were characterized by loss of CD4⁺ and CD8⁺ naïve T cells, as well as CD69⁺ T_H CM₁ cells and CD69⁺ T_H CM₂ cells, but to variable extents harboured clonally expanded CD4⁺ and CD8⁺ PD1⁺ TIM3⁺ T_{tox} cells. The latter were part of a cellular trajectory that continuously converged into terminally exhausted T cells and had lost TCF7 transcription factor activity⁴⁸. Higher proportions of these cells were associated with inferior survival in FL and DLBCL, which is in line with previous studies in DLBCL⁴⁹ or FL⁵⁰. PD1⁺ TIM3⁺ T_{tox} cells were located within several spatial neighbourhoods, thereby allowing for contact with various types of immune cell. Specifically in LNs infiltrated by DLBCL, PD1⁺ TIM3⁺ T_{tox} cells were strongly co-localized with tumour cells and macrophages, which have recently been shown to be attracted by exhausted T cells and inversely, to reinforce T cell exhaustion⁵¹. This observation might explain why DLBCL harboured the highest proportions of PD1⁺ TIM3⁺ T_{tox} cells and why higher numbers of macrophages are associated with inferior outcome in DLBCL^{52,53}.

A second trajectory was characterized by expression of PD1, absence of TIM3 and other inhibitory receptors, but maintained transcription factor activity of TCF7. Previous work suggested that only TCF7⁺ PD1⁺ T cells can be reinvigorated upon checkpoint inhibition, whereas terminally exhausted TCF7[−] T cells cannot be restored^{54,55}. This observation is of particular interest because immune checkpoint blockade is remarkably ineffective in nodal B-NHL^{56,57}, which might be—in the light of our study—due to the predominance of terminally exhausted T cells. We speculate that patients with B-NHL harbouring high levels of PD1⁺ TIM3[−] T_{tox} cells could represent a subgroup that benefits most from combining T cell-engaging immunotherapies and immune checkpoint blockade.

Beyond clonal T_{tox} cells, we found that both FL and MZL were characterized by clonal T_{FH} cells and IKZF3⁺ T_{reg} EM₂ cells, and overall had

a similar pattern of T cell infiltration. Whereas T_{FH} cells have been extensively studied and are known to support the growth of malignant B cells in FL⁴³, an enrichment of IKZF3⁺ T_{reg} EM₂ cells has, to our knowledge, neither been described in FL nor in MZL. We observed higher proportions of IKZF3⁺ T_{reg} EM₂ cells in patients with low-graded FL, suggesting that this T cell subset could modulate the proliferation capacity of malignant B cells. IKZF3⁺ T_{reg} EM₂ cells are suggested to bear strong suppressive capacity and represent an induced T_{reg} phenotype⁴⁵. Indeed, we demonstrated that IKZF3⁺ T_{reg} EM₂ cells and T_{FH} cells carry a substantial proportion of identical TCR clonotypes, which implies that IKZF3⁺ T_{reg} EM₂ cells most likely derive from T_{FH} cells. More mechanistically oriented studies are needed to clarify the role of IKZF3⁺ T_{reg} cells.

In summary, our work refines previous knowledge of lymphoma-infiltrating T cells by employing recent technological advances and offers a different perspective on various B-NHL entities. This broader yet more detailed view revealed that B-NHL entities shape their T cell microenvironment in distinct manners, which could not be readily detected in studies investigating only single entities.

Online content

Any methods, additional references, Nature Portfolio reporting summaries, source data, extended data, supplementary information, acknowledgements, peer review information; details of author contributions and competing interests; and statements of data and code availability are available at <https://doi.org/10.1038/s41556-024-01358-2>.

References

1. Bea, S. et al. Landscape of somatic mutations and clonal evolution in mantle cell lymphoma. *Proc. Natl Acad. Sci. USA* **110**, 18250–18255 (2013).
2. Chapuy, B. et al. Molecular subtypes of diffuse large B cell lymphoma are associated with distinct pathogenic mechanisms and outcomes. *Nat. Med.* **24**, 679–690 (2018).
3. Okosun, J. et al. Integrated genomic analysis identifies recurrent mutations and evolution patterns driving the initiation and progression of follicular lymphoma. *Nat. Genet.* **46**, 176–181 (2014).
4. Schmitz, R. et al. Genetics and pathogenesis of diffuse large B-cell lymphoma. *N. Engl. J. Med.* **378**, 1396–1407 (2018).
5. Spina, V. et al. The genetics of nodal marginal zone lymphoma. *Blood* **128**, 1362–1373 (2016).
6. Morin, R. D. et al. Genetic landscapes of relapsed and refractory diffuse large B-cell lymphomas. *Clin. Cancer Res.* **22**, 2290–2300 (2016).
7. Yi, S. et al. Genomic and transcriptomic profiling reveals distinct molecular subsets associated with outcomes in mantle cell lymphoma. *J. Clin. Invest.* **132**, e153283 (2022).
8. Martinez, N. et al. Whole-exome sequencing in splenic marginal zone lymphoma reveals mutations in genes involved in marginal zone differentiation. *Leukemia* **28**, 1334–1340 (2014).
9. Budde, L. E. et al. Single-agent mosunetuzumab shows durable complete responses in patients with relapsed or refractory B-cell lymphomas: phase I dose-escalation study. *J. Clin. Oncol.* **40**, 481–491 (2022).
10. Hutchings, M. et al. Glofitamab, a novel, bivalent CD20-targeting T-cell-engaging bispecific antibody, induces durable complete remissions in relapsed or refractory B-cell lymphoma: a phase I trial. *J. Clin. Oncol.* **39**, 1959–1970 (2021).
11. Locke, F. L. et al. Axicabtagene ciloleucel as second-line therapy for large B-cell lymphoma. *N. Engl. J. Med.* **386**, 640–654 (2022).
12. Roider, T. et al. An autologous culture model of nodal B-cell lymphoma identifies ex vivo determinants of response to bispecific antibodies. *Blood Adv.* **5**, 5060–5071 (2021).
13. Scott, D. W. & Gascoyne, R. D. The tumour microenvironment in B cell lymphomas. *Nat. Rev. Cancer* **14**, 517–534 (2014).

14. Papalexis, E. & Satija, R. Single-cell RNA sequencing to explore immune cell heterogeneity. *Nat. Rev. Immunol.* **18**, 35–45 (2018).

15. Suva, M. L. & Tirosh, I. Single-cell RNA sequencing in cancer: lessons learned and emerging challenges. *Mol. Cell* **75**, 7–12 (2019).

16. Roider, T. et al. Dissecting intratumour heterogeneity of nodal B-cell lymphomas at the transcriptional, genetic and drug-response levels. *Nat. Cell Biol.* **22**, 896–906 (2020).

17. Andor, N. et al. Single-cell RNA-seq of follicular lymphoma reveals malignant B-cell types and coexpression of T-cell immune checkpoints. *Blood* **133**, 1119–1129 (2019).

18. Han, G. et al. Follicular lymphoma microenvironment characteristics associated with tumor cell mutations and MHC Class II expression. *Blood Cancer Discov.* **3**, 428–443 (2022).

19. Nathan, A. et al. Multimodally profiling memory T cells from a tuberculosis cohort identifies cell state associations with demographics, environment and disease. *Nat. Immunol.* **22**, 781–793 (2021).

20. Nathan, A. et al. Multimodal single-cell approaches shed light on T cell heterogeneity. *Curr. Opin. Immunol.* **61**, 17–25 (2019).

21. Stoeckius, M. et al. Simultaneous epitope and transcriptome measurement in single cells. *Nat. Methods* **14**, 865–868 (2017).

22. Hao, Y. et al. Integrated analysis of multimodal single-cell data. *Cell* **184**, 3573–3587 e29 (2021).

23. Aibar, S. et al. SCENIC: single-cell regulatory network inference and clustering. *Nat. Methods* **14**, 1083–1086 (2017).

24. Sebzda, E. et al. Transcription factor KLF2 regulates the migration of naive T cells by restricting chemokine receptor expression patterns. *Nat. Immunol.* **9**, 292–300 (2008).

25. Kim, C. et al. The transcription factor TCF1 in T cell differentiation and aging. *Int. J. Mol. Sci.* **21**, 6497 (2020).

26. Fontenot, J. D., Gavin, M. A. & Rudensky, A. Y. Foxp3 programs the development and function of CD4⁺CD25⁺ regulatory T cells. *Nat. Immunol.* **4**, 330–336 (2003).

27. Liu, X. et al. Transcription factor achaete-scute homologue 2 initiates follicular T-helper-cell development. *Nature* **507**, 513–518 (2014).

28. Friedman, J. H. Greedy function approximation: a gradient boosting machine. *Ann. Stat.* **29**, 1189–1232 (2001).

29. Becht, E. et al. Reverse-engineering flow-cytometry gating strategies for phenotypic labelling and high-performance cell sorting. *Bioinformatics* **35**, 301–308 (2018).

30. Pai, J. A. & Satpathy, A. T. High-throughput and single-cell T cell receptor sequencing technologies. *Nat. Methods* **18**, 881–892 (2021).

31. Tirosh, I. et al. Dissecting the multicellular ecosystem of metastatic melanoma by single-cell RNA-seq. *Science* **352**, 189–196 (2016).

32. Qiu, X. et al. Reversed graph embedding resolves complex single-cell trajectories. *Nat. Methods* **14**, 979–982 (2017).

33. Hanna, B. S. et al. Interleukin-10 receptor signaling promotes the maintenance of a PD-1^{int} TCF-1⁺ CD8⁺ T cell population that sustains anti-tumor immunity. *Immunity* **54**, 2825–2841 e10 (2021).

34. Garni-Wagner, B. A. et al. A novel function-associated molecule related to non-MHC-restricted cytotoxicity mediated by activated natural killer cells and T cells. *J. Immunol.* **151**, 60–70 (1993).

35. Quigley, M. et al. Transcriptional analysis of HIV-specific CD8⁺ T cells shows that PD-1 inhibits T cell function by upregulating BATF. *Nat. Med.* **16**, 1147–1151 (2010).

36. Man, K. et al. Transcription factor IRF4 promotes CD8⁺ T cell exhaustion and limits the development of memory-like T cells during chronic infection. *Immunity* **47**, 1129–1141 e5 (2017).

37. Shin, H. et al. A role for the transcriptional repressor Blimp-1 in CD8⁺ T cell exhaustion during chronic viral infection. *Immunity* **31**, 309–320 (2009).

38. Li, J. et al. High levels of eomes promote exhaustion of anti-tumor CD8⁺ T cells. *Front. Immunol.* **9**, 2981 (2018).

39. Newman, A. M. et al. Determining cell type abundance and expression from bulk tissues with digital cytometry. *Nat. Biotechnol.* **37**, 773–782 (2019).

40. Roussel, M. et al. Functional characterization of PD1⁺TIM3⁺ tumor-infiltrating T cells in DLBCL and effects of PD1 or TIM3 blockade. *Blood Adv.* **5**, 1816–1829 (2021).

41. Marcus, R. et al. Obinutuzumab for the first-line treatment of follicular lymphoma. *N. Engl. J. Med.* **377**, 1331–1344 (2017).

42. Bolen, C. R. et al. Treatment dependence of prognostic gene expression signatures in de novo follicular lymphoma. *Blood* **137**, 2704–2707 (2021).

43. Mintz, M. A. & Cyster, J. G. T follicular helper cells in germinal center B cell selection and lymphomagenesis. *Immunol. Rev.* **296**, 48–61 (2020).

44. Thornton, A. M. et al. Expression of Helios, an Ikaros transcription factor family member, differentiates thymic-derived from peripherally induced Foxp3⁺ T regulatory cells. *J. Immunol.* **184**, 3433–3441 (2010).

45. Scarlata, C. M. et al. Differential expression of the immunosuppressive enzyme IL4I1 in human induced Aiolos⁺, but not natural Helios⁺, FOXP3⁺ Treg cells. *Eur. J. Immunol.* **45**, 474–479 (2015).

46. Sage, P. T. & Sharpe, A. H. T follicular regulatory cells. *Immunol. Rev.* **271**, 246–259 (2016).

47. Schurch, C. M. et al. Coordinated cellular neighborhoods orchestrate antitumoral immunity at the colorectal cancer invasive front. *Cell* **182**, 1341–1359 e19 (2020).

48. Blank, C. U. et al. Defining 'T cell exhaustion'. *Nat. Rev. Immunol.* **19**, 665–674 (2019).

49. Zhang, T. et al. Genetic mutations of Tim-3 ligand and exhausted Tim-3⁺ CD8⁺ T cells and survival in diffuse large B cell lymphoma. *J. Immunol. Res.* **2020**, 6968595 (2020).

50. Yang, Z. Z. et al. Expression of LAG-3 defines exhaustion of intratumoral PD-1⁺ T cells and correlates with poor outcome in follicular lymphoma. *Oncotarget* **8**, 61425–61439 (2017).

51. Kersten, K. et al. Spatiotemporal co-dependency between macrophages and exhausted CD8⁺ T cells in cancer. *Cancer Cell* **40**, 624–638 e9 (2022).

52. Li, Y. L. et al. Tumor-associated macrophages predict prognosis in diffuse large B-cell lymphoma and correlation with peripheral absolute monocyte count. *BMC Cancer* **19**, 1049 (2019).

53. Nam, S. J. et al. An increase of M2 macrophages predicts poor prognosis in patients with diffuse large B-cell lymphoma treated with rituximab, cyclophosphamide, doxorubicin, vincristine and prednisone. *Leuk. Lymphoma* **55**, 2466–2476 (2014).

54. Siddiqui, I. et al. Intratumoral Tcf1⁺PD-1⁺CD8⁺ T cells with stem-like properties promote tumor control in response to vaccination and checkpoint blockade immunotherapy. *Immunity* **50**, 195–211 e10 (2019).

55. Miller, B. C. et al. Subsets of exhausted CD8⁺ T cells differentially mediate tumor control and respond to checkpoint blockade. *Nat. Immunol.* **20**, 326–336 (2019).

56. Armand, P. et al. Efficacy and safety results from CheckMate 140, a phase 2 study of nivolumab for relapsed/refractory follicular lymphoma. *Blood* **137**, 637–645 (2021).

57. Ansell, S. M. et al. Nivolumab for relapsed/refractory diffuse large B-cell lymphoma in patients ineligible for or having failed autologous transplantation: a single-arm, phase II study. *J. Clin. Oncol.* **37**, 481–489 (2019).

Open Access This article is licensed under a Creative Commons Attribution 4.0 International License, which permits use, sharing, adaptation, distribution and reproduction in any medium or format, as long as you give appropriate credit to the original author(s) and the source, provide a link to the Creative Commons license, and indicate if changes were made. The images or other third party material in this article are included in the article's Creative Commons license, unless indicated otherwise in a

credit line to the material. If material is not included in the article's Creative Commons license and your intended use is not permitted by statutory regulation or exceeds the permitted use, you will need to obtain permission directly from the copyright holder. To view a copy of this license, visit <http://creativecommons.org/licenses/by/4.0/>.

© The Author(s) 2024

¹Department of Medicine V, Hematology, Oncology and Rheumatology, University of Heidelberg, Heidelberg, Germany. ²Molecular Medicine Partnership Unit, Heidelberg, Germany. ³European Molecular Biology Laboratory, Heidelberg, Germany. ⁴Department of Microbiology and Immunology, Stanford University School of Medicine, Stanford, CA, USA. ⁵Clinical Cooperation Unit Molecular Hematology/Oncology, German Cancer Research Center, Heidelberg, Germany. ⁶Division of Molecular Genetics, German Cancer Research Center, Heidelberg, Germany. ⁷Molecular Pathology of Lymphoid Neoplasms, Fundació de Recerca Clínic Barcelona-Institut d'Investigacions Biomèdiques August Pi i Sunyer (FRCB-IDIBAPS), Barcelona, Spain.

⁸Department of Hematology and Oncology, University Hospital Düsseldorf, Düsseldorf, Germany. ⁹Genomics and Transcriptomics Laboratory, University of Düsseldorf, Düsseldorf, Germany. ¹⁰National Center for Tumor Diseases, Heidelberg, Germany. ¹¹German Cancer Research Center, Heidelberg, Germany. ¹²Department of Pathology and Neuropathology, University Hospital and Comprehensive Cancer Center Tübingen, Tübingen, Germany.

¹³Department of Medicine III, Laboratory for Experimental Leukemia and Lymphoma Research, Ludwig-Maximilians-University Hospital, Munich, Germany.

¹⁴Department of Pathology, University of Heidelberg, Heidelberg, Germany. ¹⁵German Cancer Consortium, Munich, Germany. ¹⁶Department of Pathology, Stanford University School of Medicine, Stanford, CA, USA. ¹⁷Center for Integrated Oncology Aachen-Bonn-Cologne-Düsseldorf (CIO ABCD), Aachen Bonn Cologne Düsseldorf, Germany. ¹⁸These first authors contributed equally: Tobias Roider, Marc A. Baertsch. ¹⁹These authors jointly supervised this work: Wolfgang Huber, Sascha Dietrich.  e-mail: wolfgang.huber@embl.de; sascha.dietrich@embl.de

Methods

LN samples

Our study was approved by the Ethics Committee of the University of Heidelberg (S-254/2016). Informed consent of all patients was obtained in advance. As collection of LN samples was part of routine diagnostic procedures, participants were not compensated. LN patient samples were processed and frozen until further analysis⁵⁸. In brief, whole LNs were cut into small pieces of approximately 1–2 mm size. LN cells were gently washed out by rinsing the pieces several times. After centrifugation, cells were frozen until further analysis. We did not include LN samples that showed obvious contamination of red blood cells after isolation. Also, samples from patients after allogeneic stem cell transplantation, chimaeric antigen receptor T cell or bispecific antibody therapy were not used in this study to minimize treatment-associated effects on the T cell microenvironment. For the same reason, samples were collected earliest 3 months after cessation of the last treatment.

Single-cell 3' RNA-seq and epitope expression profiling

Cells were thawed and immediately washed to remove dimethyl sulfoxide. To prevent entity-associated batch effects, samples were processed in batches of four to five containing at least three different entities. After thawing, we applied a dead cell removal kit (Miltenyi Biotec, 130-090-101) to all samples to reach a viability of at least 85–90%. Samples not reaching a viability above 85% were excluded. Then, 5×10^5 viable cells were stained by a pre-mixed cocktail of oligonucleotide-conjugated antibodies (Supplementary Table 2) and incubated at 4 °C for 30 min. Cells were washed three times with ice-cold washing buffer and each time centrifuged at 4 °C for 5 min. After completion, cells were counted and viability was determined again. Samples not reaching a viability above 85% were excluded. The preparation of the bead-cell suspensions, synthesis of complementary DNA and single-cell gene expression and antibody-derived tag (ADT) libraries were performed using a Chromium single-cell v3.13' kit (10x Genomics, 1000269) according to the manufacturer's instructions.

Single-cell 5' RNA-seq and TCR repertoire profiling

Apart from epitope staining, sample processing was identical to 3' scRNA-seq. The preparation of the bead-cell suspensions, synthesis of complementary DNA and single-cell gene expression and TCR libraries were performed using a Chromium single-cell v2 5' and human TCR amplification kit (both 10x Genomics, 1000265, 1000252) according to the manufacturer's instructions.

Single-cell library sequencing and data processing

The 3' gene expression and ADT libraries were pooled in a ratio of 3:1 aiming for 40,000 reads (gene expression) and 15,000 reads per cell (ADT), respectively. Sequencing was performed on a NextSeq 500 (Illumina). 5' gene expression libraries were sequenced on a NextSeq 2000 (Illumina) aiming for 50,000 reads per cell. TCR libraries were sequenced on a NextSeq 500 (Illumina) aiming for a minimum of 5,000 reads per cell. After sequencing, the Cell Ranger (10x Genomics, v6.1.1) function cellranger mkfastq was used to demultiplex and to align raw base-call files to the reference genome (hg38). For 3' gene and epitope expression libraries, the obtained FASTQ files were counted by the cellranger count command, whereas cellranger multi was used for 5' gene expression and TCR libraries. As reference for TCR libraries, the VDJ ensembl reference (hg38, v5.0.0) was used. If not otherwise indicated, default settings were used for all functions.

Analysis and integration of CITE-seq data

The R package Seurat (v4.1.0) was used to perform data quality control, filtering, and normalization. Gene counts per cell, ADT counts per cell and percentages of mitochondrial reads were computed using the built-in functions. PCA, shared nearest neighbour-based clustering and UMAP were done on the basis of the combined transcriptome and

epitope data. After mapping the CD3 and CD19 epitope expression, non-T-cell clusters and doublets were removed. For data integration across the different preparation batches, we used the IntegrateData function of the Seurat package. For multimodal clustering based on gene and epitope expression, the weighted nearest neighbour approach was used²². To estimate the proportion of positive cells for each surface marker, we calculated the denoised protein expression using the totalVI Python package⁵⁹.

Inferring transcription factor activity on the basis of single-cell gene expression

We used the SCENIC (Single-Cell rEgulatory Network Inference and Clustering) package²³ to infer gene regulatory networks and transcription factor activity on the basis of scRNA-seq data. Functions were used according to publicly available vignettes.

Surface and intracellular flow cytometry staining

LN-derived cells were thawed and stained for viability using a fixable viability dye e506 (Thermo Fisher Scientific, 65-0866-14) and for different surface markers depending on the experimental set-up. The following surface antibodies were used: anti-CD3-PerCP-Cy5.5, anti-CD4-PE-Dazzle, anti-CD8-APC-Cy7, anti-CD45RA-FITC, anti-CD25-BV421, anti-CD31-BV605, anti-CXCR5-BV711, anti-TIM3-BV711, anti-CD278-BV605, anti-PD1-PE-Cy7, anti-CD69-AF700 and anti-CD244-BV421 (all BioLegend, Supplementary Table 4). For subsequent intracellular staining, cells were fixed and permeabilized with the intracellular fixation/permeabilization buffer set (Thermo Fisher Scientific, 88-8824-00) and stained with anti-Ki67-BV785, anti-FOXP3-AF647, anti-IKZF3-PE or adequate isotype controls (Thermo Fisher Scientific, BD Biosciences, Supplementary Table 4). Then, cells were analysed using an LSR Fortessa (BD Biosciences) and FACSDiva (BD Biosciences, version 8). For analysis and gating of flow cytometry data, FlowJo (v10.8.0) was used.

Multinomial classification of T cell subpopulations

First, we evaluated whether multimodally defined T cell subsets can be distinguished in general by using surface markers only. Therefore, we trained gradient boosting models ('xgbTree')²⁸ on the basis of surface marker expression of single-cell data. To reduce data load, only 30% of all cells were used. Tenfold cross-validation was employed to optimize the model. Since surface marker were not sufficient to reach sufficient accuracy, additional models were trained using surface marker plus gene expression of MKI67, IKZF3 and FOXP3, since these genes were differentially expressed between T cell subsets that could not be sufficiently predicted using only surface proteins. Finally, markers were ranked and selected by their variable importance to build flow cytometry panels. In case two or more markers deliver similar information (for example, CD95 and CD45RA), only one was selected. Gating strategies were built using the R package hypergate²⁹ and optimized in an iterative process. The final gating strategy for all multimodally defined T cell subsets is illustrated in Supplementary Figs. 1 and 2.

Prediction of B-NHL entity from T cell proportions

To assess feasibility of predicting B-NHL entity or tumour-free condition based on the proportions of all T cell subsets and overall T cell frequency, we trained classifiers based on multivariate regression with L1 penalty (LASSO) implemented in the R package glmnet (v4.1)⁶⁰. The hyperparameter lambda was determined using cv.glmnet with balanced folds and weights inversely proportional to class size. The confusion matrix was computed using leave-one-out cross-validation.

Analysis of TCR diversity

To estimate the diversity of the TCR repertoire on the basis of scTCR profiling, we employed the R package immunarch (v0.8.0; <https://immunarch.com/>) on the output files of the cellranger pipeline.

TCR diversity across samples was compared using a rarefaction analysis. Therefore, the function `repDiversity` with method = 'raref' was applied.

Mapping of 5' scRNA-seq data onto CITE-seq reference data

To evaluate scTCR data in the context of multimodally defined T cell subsets, 5' scRNA-seq data were mapped onto the CITE-seq reference data, using the built-in functions `FindTransferAnchors` and `MapQuery` of the Seurat package (v4.1.0). The mapping accuracy was evaluated by comparing the T cell subset proportion of 5' and 3' data of the identical patient sample.

Pseudotime analysis and exhaustion signature

Pseudotime analysis based on gene expression profiles of T_{tox} cells was performed using the monocle3 package³². In brief, the Seurat object was converted into a cell dataset. Trajectory and pseudotime analysis were performed using the functions `learn_graph` and `order_cells`, respectively. As root cells, naive CD8⁺ T cells were selected. Minimal branch length was set to 10; otherwise, default settings were used.

To define a transcriptional module for T cell exhaustion, differentially expressed genes of terminally exhausted T cells, meaning T_{tox} cells with highest levels of inhibitory receptors and decreasing expression of effector molecules (Fig. 5c), were determined (Supplementary Table 5). The UCell package (v1.3.1)⁶¹, which is based on the Mann–Whitney *U* statistic, was then applied to calculate an exhaustion score for each cell.

Deconvolution of bulk RNA sequencing data

Deconvolution of bulk RNA-seq data was performed using the interactive web application (<https://cibersortx.stanford.edu/>) developed by Newman and colleagues³⁹. First, a signature matrix was created on the basis of the scRNA-seq data and the cluster annotation as cell types. Minimum expression was set to zero, and 200 replicates were used. Otherwise, default settings were applied to create a signature matrix. Second, cell fractions were imputed using bulk RNA-seq data and signature matrix as input. S-mode batch correction and absolute mode was used for each analysis.

Survival analysis

Survival data were obtained only from previously published data or studies^{2,4,41}. Analysis of the progression-free survival probability was performed in combination with the estimated cell type proportions using deconvolution of bulk RNA-seq data. To divide the data into two groups (low and high), we determined a cut-off based on the maximized *P* value of a log-rank test using the `maxstat` R package (v0.7.25). Kaplan–Meier curves were drawn using the `survminer` R package (v0.4.9).

Tissue microarray and coverslip preparation

Representative tumour or tumour-free LN areas in archival FFPE tissue blocks from 19 patients (Extended Data Fig. 1a and Supplementary Table 1) were selected by board-certified pathologists of the Tissue Bank of the National Center for Tumor Diseases and Institute of Pathology at the University Hospital Heidelberg. Tissue microarrays (TMAs) containing two 4.5-mm cores per patient were generated. TMA sections (4 μm) were mounted onto Vectabond-precoated 25 \times 25 mm coverslips and coated in paraffin for storage until staining⁶².

Antibody conjugation, validation and titration

Multicolour immunofluorescence was performed using the CODEX approach⁴⁷. Antibodies used for CODEX experiments are summarized in Supplementary Table 6. Purified, carrier-free antibodies (50–100 μg per reaction) were reduced with tris(2-carboxyethyl)phosphine and conjugated at 1:2 weight/weight ratio to maleimide-modified CODEX DNA oligonucleotides, which were purchased from TriLink Biotechnologies and deprotected via retro-Diels–Alder reaction.

Conjugated antibodies were first evaluated in CODEX singleplex stains on tonsil and/or lymphoma tissue by comparison with online databases (The Human Protein Atlas, Pathology Outlines), immunohistochemical reference stains and/or published literature under the supervision of a board-certified pathologist. Staining patterns were validated in multiplex experiments in the presence of positive and negative control antibodies and the appropriate dilution of each antibody was titrated starting from 1:100 to optimize signal-to-noise ratio.

Multiplex tissue staining and fixation

Coverslips were deparaffinized, rehydrated and submitted to heat-induced epitope retrieval at pH 9 (Dako target retrieval solution, S236784-2, Agilent) and 97 °C for 10 min in a Lab Vision PT module (Thermo Fisher). After blocking of non-specific binding with CODEX FFPE blocking solution, coverslips were stained overnight with the full antibody panel at the dilutions given in Supplementary Table 6 in CODEX FFPE blocking solution⁶³ in a sealed humidity chamber at 4 °C on a shaker. Coverslips were then fixed with 1.6% paraformaldehyde, followed by methanol and BS3 fixative (Thermo Fisher) before storage in CODEX buffer S4 until imaging⁶³.

Multicycle imaging

Stained coverslips were mounted onto custom acrylic plates (Pololou Corporation) with mounting gaskets (Qintay), thereby creating a flow cell with a surface area of 19 \times 19 mm above the tissue for fluid exchange. Acrylic plates were inserted into a Keyence BZ-X710 inverted fluorescence microscope equipped with a CFI Plan Apo λ 20 \times /0.75 objective (Nikon) using custom adapters. For each core an area of 7 \times 7 fields of view (30% overlap between tiles) and an adequate number of *z* planes (10–14) required to capture the best focal plane across the imaging area were selected. Multicycle imaging was performed using a CODEX microfluidics device and CODEX driver software v1.29.0.1 (Akoya Biosciences). Exposure times and assignment of markers to imaging cycles and fluorescent channels are provided in Supplementary Table 6. After completion of multicycle imaging, coverslips were stained with haematoxylin–eosin, and the same areas were imaged in brightfield mode.

Image processing

Raw TIFF images were processed using the RAPID pipeline⁶⁴ in MATLAB (version R2020a) with the following settings: *nCyc* = 51, *nReg* = number of regions imaged (depending on TMA), *nTil* = 49, *nZ* = number of *z*-planes imaged (depending on TMA), *nCh* = [1,4], *nTilRow* = 7, *nTilCol* = 7, *overlapRatio* = 0.3, *reg_range* = 1:*nReg*, *cyc_range* = 1:*nCyc*, *til_range* = 1:*nTil*, *cpu_num* = depending on computer system used, *neg_flag* = 1, *gpu_id* = depending on number of GPUs available, *cyc_bg* = 1. After deconvolution (two iterations), best focal plane selection, lateral drift compensation, stitching of individual images and background subtraction, processed images were concatenated to hyperstacks. All tissue cores were checked visually for staining quality of each antibody in ImageJ/Fiji (version 1.53q).

Cell segmentation and cell type annotation

Individual nuclei were segmented on the basis of the Hoechst stain (cycle 1), derived nuclear masks were dilated, and cellular marker expression levels were quantified using a modified version of the Mask region-convolutional neural network-based CellSeg software⁶⁵ run on the full-resolution RAPID stitched images with the following parameters: *GROWTH_PIXELS_PLANE* = 1.0, *output_adjacency_quant* = True, *BOOST* = 1, *OVERLAP* = 80, *MIN_AREA* = 80, *INCREASE_FACTOR* = 4.0, *AUTOBOOST_PERCENTILE* = 99.98. A threshold based on the intensity of the nuclear markers Hoechst and DRAQ5 was used to exclude non-cellular events and remove cells from tissue areas of low image quality. Marker expression levels compensated for lateral spillover were used for further analysis and the range of each marker was *z*

normalized per imaging run. A total of $n = 5,690,284$ cells were submitted to an initial round of Leiden-based clustering ($n_{\text{neighbors}} = 10$, resolution = 2) on key phenotypic markers (CD11b, CD11c, CD14, CD15, CD16, CD163, CD20, CD206, CD21, CD25, CD3, CD31, CD34, CD38, CD4, CD45, CD5, CD56, CD57, CD68, CD7, CD79a, CD8, CD90, FOXP3, HLA-DR, kappa light chain, lambda light chain, MCT, PAX5 and PDPN) using the scanpy Python package^{66,67}. Each of the resulting clusters ($n = 55$) was assessed for purity of its cell type composition on the basis of marker expression and overlays of the cells in each cluster onto image hyperstacks using CODEX scripts for ImageJ/Fiji (available at ref. 68). Clusters were merged, split and/or further subclustered as appropriate to define broad cell types (for example, T cells, B cells and so on). This process was repeated within these cell types using additional markers as appropriate to annotate more granular cell subsets. Briefly, marker combinations used for cell typing of non-T cells include CD16, CD68, CD163, CD206 and HLA-DR (macrophages); CD11c, CD68 and HLA-DR (DC); CD15 (granulocytes); MCT and GRZB (mast cells); CD34, CD31, CD90 and PDPN (stromal cells); PDPN and CD21 (FDC); CD56 (NK and NK T cells); CD38, CD31, and kappa and lambda light chain (plasma cells); PAX5, CD20 and CD79a (B cells). Further, T cell subsets were derived on the basis of key subset markers (CD45, CD45RA, CD45RO, CD3, CD5, CD7, CD4, CD8, FOXP3, CXCR5, CXCL13, PD1, TIM3, CD31 and Ki67) and were validated using expression of additional T cell markers in the panel and overlays onto image hyperstacks.

Neighbourhood and nearest neighbour analysis

Neighbourhood analysis was modified based on a previously described approach⁴⁷. For each cell of the joint highly multiplexed immunofluorescence data, the 25 nearest neighbours were determined on the basis of their Euclidean distance of the x and y coordinates, resulting in one ‘window’ of cells per individual cell. Next, these windows were grouped using k -means clustering based on the cell type proportions within each window. Finally, each cell was annotated by the neighbourhood of its surrounding ‘window’. $k = 10$ was selected on the basis of the overlays of the neighbourhood assignments with the original fluorescent and haematoxylin–eosin-stained images. Higher values of k did not result in an improved biologically interpretable number of neighbourhoods.

Interactive browsing of highly multiplexed immunofluorescence data

All tissue cores imaged in this study including staining of 52 different markers are available for interactive browsing at <http://45.88.80.143:8501/>.

Statistics and reproducibility

Statistical analysis and data illustration was performed in R (v4.2.1) using the R packages glmnet (v4.1-2), ggplotify (v0.1.0), maxstat (v0.7-25), R.oo (v1.24.0), rstatix (v0.7.0), viridis (v0.6.2), dplyr (v1.0.10), tidyverse (v1.3.1), FNN (v1.1.3), Matrix (v1.5-1), ggraph (v2.0.6), survival (v3.2-13), R.methodsS3 (v1.8.1), ggpubr (v0.4.0), viridisLite (v0.4.1), purrr (v0.3.4), future.apply (v1.8.1), immunarch (v0.7.0), igraph (v1.3.5), survminer (v0.4.9), readxl (v1.4.1), ggrepel (v0.9.1), SeuratObject (v4.0.4), readr (v2.1.2), future (v1.23.0), data.table (v1.14.2), ggrastr (v1.0.1), ggridges (v0.5.3), caret (v6.0-90), matrixStats (v0.61.0), Seurat (v4.1.0), tidyverse (v1.2.1), pamr (v1.56.1), dtplyr (v1.2.2), ggtext (v0.1.1), cowplot (v1.1.1), lattice (v0.20-45), scales (v1.2.1),forcats (v0.5.1), tibble (v3.1.8), cluster (v2.1.2), rmdformats (v1.0.4), ggalluvial (v0.12.3), R.utils (v2.11.0), patchwork (v1.1.2), RColorBrewer (v1.1-3), stringr (v1.4.1) and ggplot2 (v3.3.6). The computational codes to exactly reproduce all analysis steps and figures is provided below (see ‘Code availability statement’). No statistical method was used to determine sample size before data collection. No data were excluded from the analyses. The experiments were not randomized. The investigators were not blinded to allocation during experiments and outcome assessment.

Reporting summary

Further information on research design is available in the Nature Portfolio Reporting Summary linked to this article.

Data availability

RNA-seq, epitope and TCR data that support the findings of this study have been deposited in the Gene Expression Omnibus (GEO) under accession codes [GSE252608](https://www.ncbi.nlm.nih.gov/geo/studies/GSE252608) and [GSE252455](https://www.ncbi.nlm.nih.gov/geo/studies/GSE252455). Highly multiplexed immunofluorescence images will be available in the BioStudies database (<https://www.ebi.ac.uk/biostudies/>) under accession number [S-BIAD565](https://www.ebi.ac.uk/biostudies/studies/S-BIAD565) (ref. 69). Flow cytometry data have been deposited in figshare under <https://doi.org/10.6084/m9.figshare.24915633>. Source data are provided with this paper.

Code availability

The computational codes, in the form of Rmarkdown documents, for reproducing all figures are available on GitHub (<https://github.com/Huber-group-EMBL/CITEseqLN-Tcells>).

References

58. Roider, T., Brinkmann, B. J. & Dietrich, S. Processing human lymph node samples for single-cell assays. *STAR Protoc.* **2**, 100914 (2021).
59. Gayoso, A. et al. Joint probabilistic modeling of single-cell multi-omic data with totalVI. *Nat. Methods* **18**, 272–282 (2021).
60. Friedman, J., Hastie, T. & Tibshirani, R. Regularization paths for generalized linear models via coordinate descent. *J. Stat. Softw.* **33**, 1–22 (2010).
61. Andreatta, M. & Carmona, S. J. UCell: robust and scalable single-cell gene signature scoring. *Comput Struct. Biotechnol. J.* **19**, 3796–3798 (2021).
62. Economou, M. et al. Proper paraffin slide storage is crucial for translational research projects involving immunohistochemistry stains. *Clin. Transl. Med* **3**, 4 (2014).
63. Black, S. et al. CODEX multiplexed tissue imaging with DNA-conjugated antibodies. *Nat. Protoc.* **16**, 3802–3835 (2021).
64. Lu, G. et al. A real-time GPU-accelerated parallelized image processor for large-scale multiplexed fluorescence microscopy data. *Front. Immunol.* **13**, 981825 (2022).
65. Lee, M. Y. et al. CellSeg: a robust, pre-trained nucleus segmentation and pixel quantification software for highly multiplexed fluorescence images. *BMC Bioinform.* **23**, 46 (2022).
66. Wolf, F. A., Angerer, P. & Theis, F. J. SCANPY: large-scale single-cell gene expression data analysis. *Genome Biol.* **19**, 15 (2018).
67. Hickey, J. W. et al. Strategies for accurate cell type identification in CODEX multiplexed imaging data. *Front. Immunol.* **12**, 727626 (2021).
68. CODEX-fiji-scripts. *GitHub* <https://github.com/bmyury/CODEX-fiji-scripts>
69. Ellenberg, J. et al. A call for public archives for biological image data. *Nat. Methods* **15**, 849–854 (2018).

Acknowledgements

T.R. was supported by a fellowship of the German Federal Ministry of Education and Research (BMBF) and a physician scientist fellowship of the Medical Faculty of University Heidelberg. M.A.B. was supported by a Career Development award of the International Myeloma Society (IMS). D.F. was supported by the PhD programme of the European Molecular Biology Laboratory (EMBL). H.V. was supported by a fellowship of the German Federal Ministry of Education and Research (BMBF). N.L. was supported by a Heidelberg School of Oncology (HSO2) fellowship from the National Center for Tumor Diseases (NCT) Heidelberg. O.W. is supported by an Else-Kröner Excellence Fellowship from the Else-Kröner-Fresenius Stiftung (Project-ID 2021_EKES13). Martina S. was supported by a grant of the Deutsche Forschungsgemeinschaft (DFG). S.D. was supported by a grant of the Hairy Cell Leukemia Foundation, the Heidelberg Research Centre for

Molecular Medicine (HRCMM) and an e:med junior group grant of the German Federal Ministry of Education and Research (BMBF). For the data management we thank the Scientific Data Storage Heidelberg (SDS@hd) which is funded by the state of Baden-Württemberg and a DFG grant (INST 35/1314-1 FUGG). We thank C. Kolb (University Hospital Heidelberg) and the EMBL flow core facility, and the DKFZ Single-Cell Open Lab (scOpenLab) for their excellent (technical) assistance. The GALLIUM study (NCT01332968) was sponsored by F. Hoffmann-La Roche.

Author contributions

Conceptualization, T.R., M.A.B., W.H. and S.D.; software, H.V.; validation, T.R., M.A.B., L.L.-C., C.M.S. and Martina S.; formal analysis, T.R., M.A.B., D.F., H.V., F.C., A.M., V.P. and W.H.; investigation, T.R., M.A.B., D.F., M.K., B.F., M.H., T.L. and Marc S.; resources, P.-M.B., N.L., A.B., G.M., C.M.-T., O.W., G.P.N., W.H. and S.D.; writing—original draft, T.R., M.A.B., B.J.B., W.H. and S.D.; writing—review and editing, all; visualization, T.R. and W.H.; supervision, T.R., C.M.S., G.P.N., W.H. and S.D.; project administration, T.R., W.H. and S.D.; funding acquisition, G.P.N., W.H. and S.D.

Funding

Open access funding provided by European Molecular Biology Laboratory (EMBL).

Competing interests

C.M.S. is a scientific advisor to, has stock options in and has received research funding from Enable Medicine, Inc. G.P.N. is a co-founder and stockholder of Akoya Biosciences, Inc. and inventor on patent US9909167 (On-slide staining by primer extension). The remaining authors declare no competing interests.

Additional information

Extended data is available for this paper at <https://doi.org/10.1038/s41556-024-01358-2>.

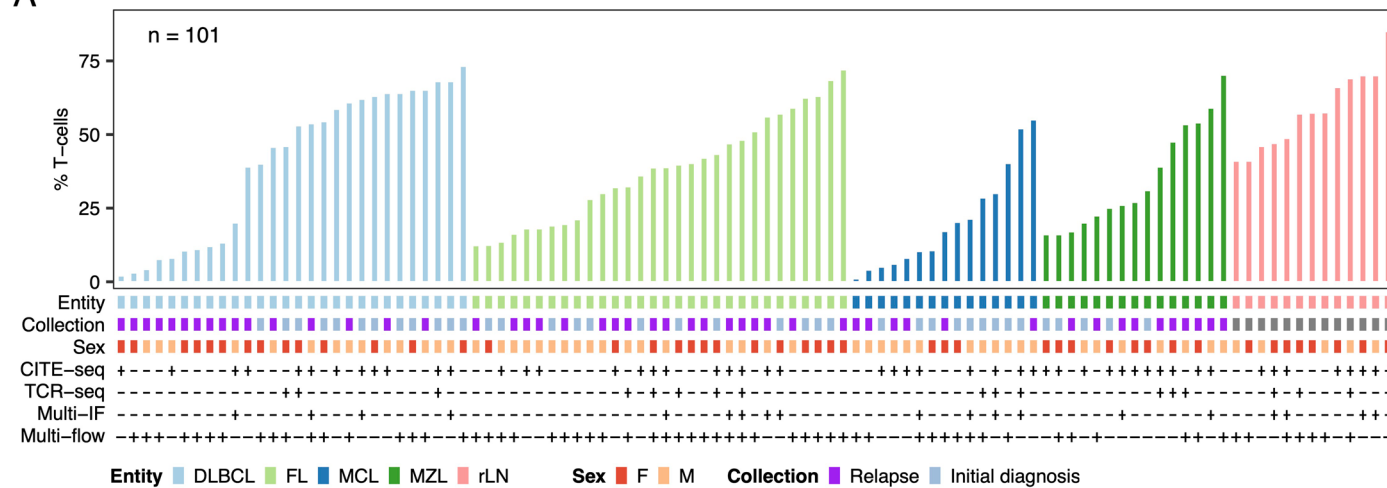
Supplementary information The online version contains supplementary material available at <https://doi.org/10.1038/s41556-024-01358-2>.

Correspondence and requests for materials should be addressed to Wolfgang Huber or Sascha Dietrich.

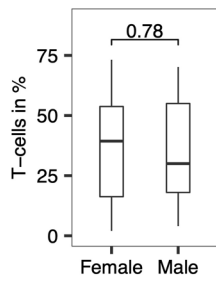
Peer review information *Nature Cell Biology* thanks Ralf Küppers, Guoji Guo and the other, anonymous, reviewer(s) for their contribution to the peer review of this work.

Reprints and permissions information is available at www.nature.com/reprints.

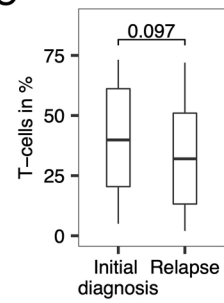
A



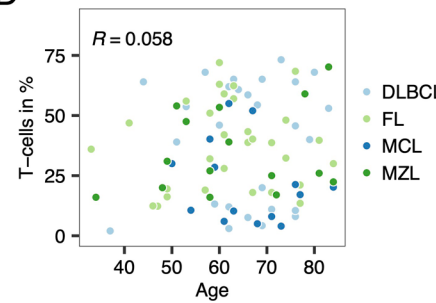
B



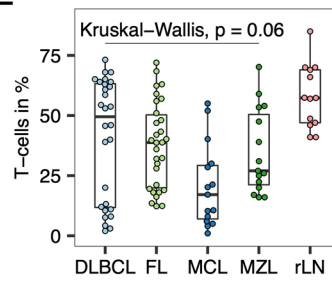
C



D



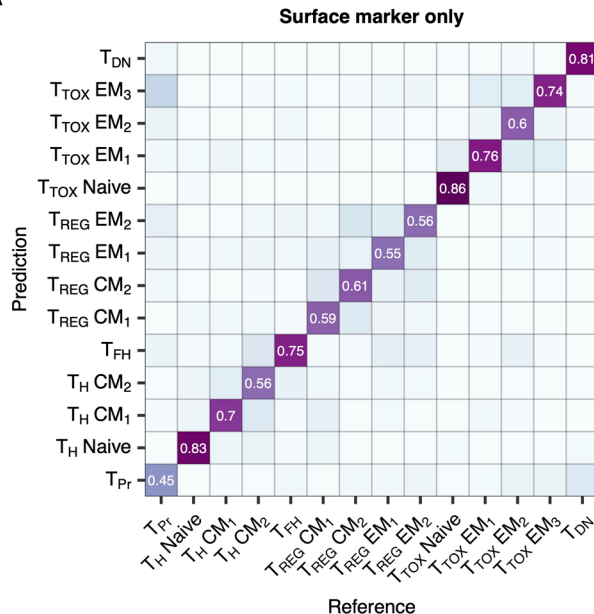
E



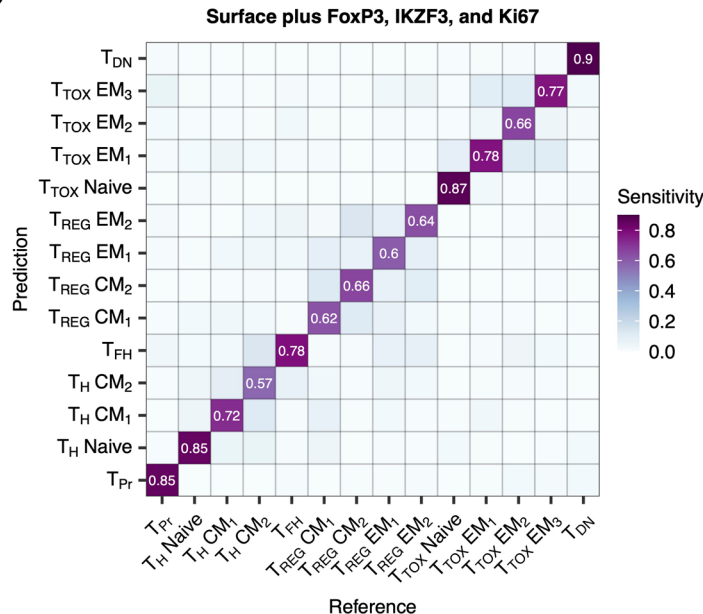
Extended Data Fig. 1 | Basic patient characteristics. **a**) Overview showing entity, pre-treatment status, sex, assay availability and the overall T-cell proportion of a total 101 lymph node samples used in this study. **b-e**) Box or scatter plots illustrating the associations of patient characteristics in n = 101 biologically independent patient samples with the overall T-cell proportion

determined by flow cytometry. P values and/or correlation coefficients were calculated using the two-sided Wilcoxon-test (B, C), Pearson's linear correlation (D) or Kruskal-Wallis-test (E). Box plots: centre line, median; box limits, first and third quartile; whiskers, 1.5 x interquartile range.

A

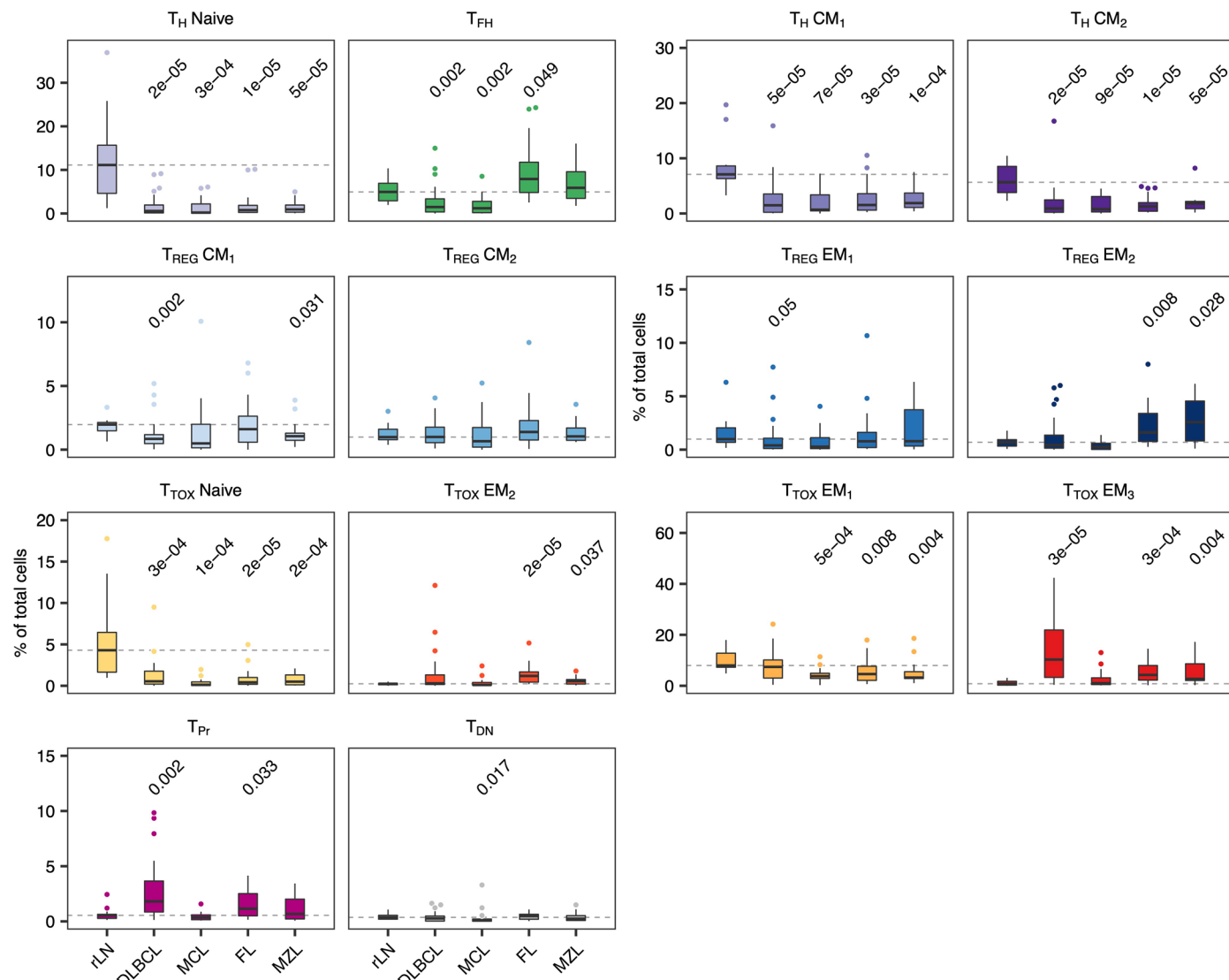


B

**Extended Data Fig. 2 | Confusion tables comparing flow cytometry and CITE-seq. a-b)**

Gradient boosting classifiers were trained and tested to evaluate whether T-cell subsets identified by CITE-seq can be predicted on basis of surface markers (A) or surface markers and differentially expressed intracellular markers accessible by flow cytometry (B, FoxP3, IKZF3, Ki67). Shown is the proportion of

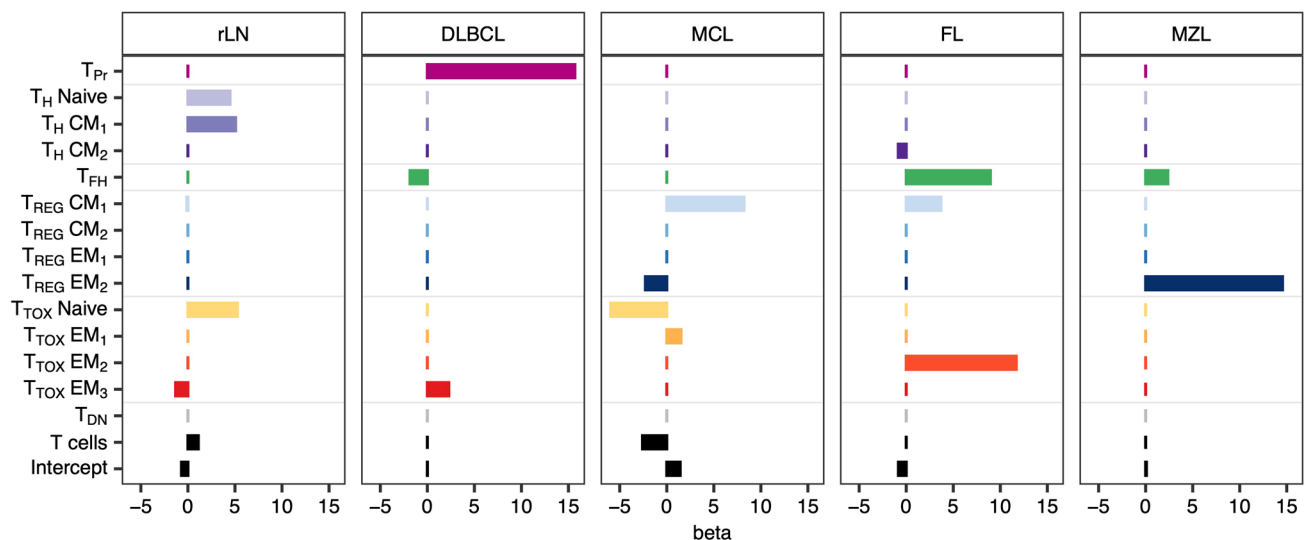
correctly predicted cells per T-cell subset across the complete CITE-seq data set ($n = 51$ byles). T_{Pr}: Proliferating T-cells. T_H: Helper T-cells. T_{FH}: Follicular helper T-cells. T_{REG}: Regulatory T-cells. T_{TOX}: Cytotoxic T-cells. T_{DN}: Double negative T-cells. CM: Central memory. EM: Effector memory.



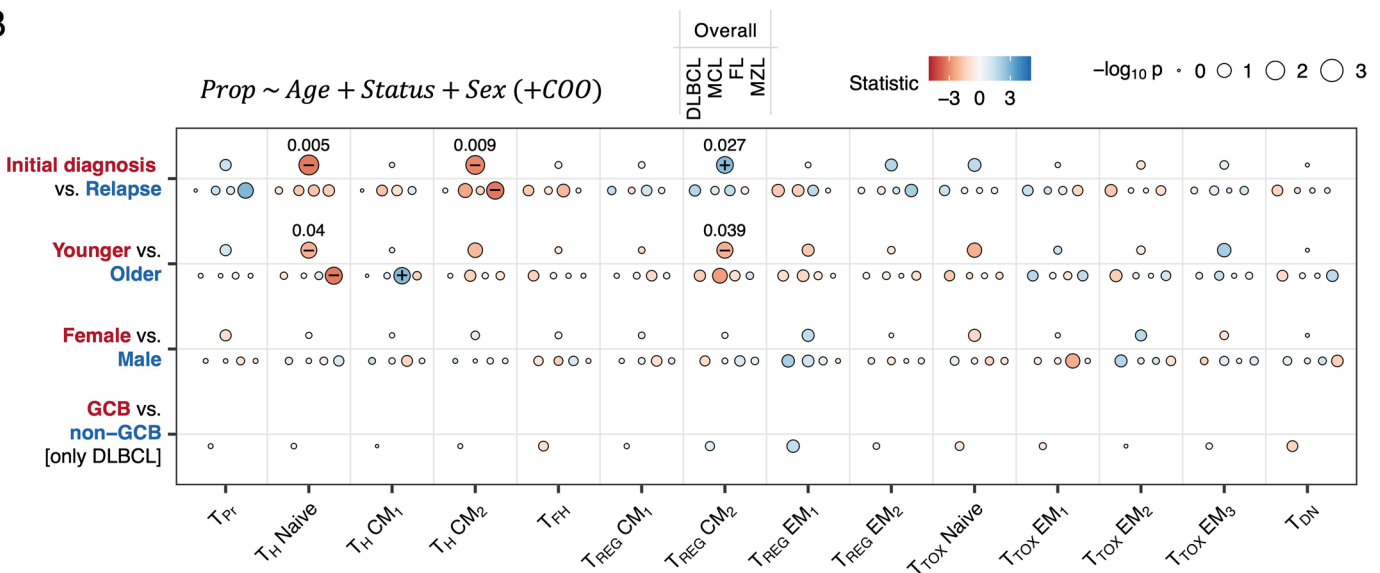
Extended Data Fig. 3 | Overall frequencies of T-cell subsets determined by CITE-seq or flow cytometry. Overall frequencies of T-cell subsets determined by CITE-seq or flow cytometry are illustrated in box plots ($n = 101$). Outliers are shown as individual dots. Each entity and subset were tested versus rLN using a two-sided Wilcoxon-test. P values were corrected for multiple testing using the Benjamini-Hochberg procedure. Only p values ≤ 0.05 are shown. Dashed

lines indicate the median of rLN. rLN: Tumor-free lymph nodes. T_{Pr} : Proliferating T-cells. T_H : Helper T-cells. Box plots: centre line, median; box limits, first and third quartile; whiskers, $1.5 \times$ interquartile range. T_{FH} : Follicular helper T-cells. T_{REG} : Regulatory T-cells. T_{TOX} : Cytotoxic T-cells. T_{DN} : Double negative T-cells. CM: Central memory. EM: Effector memory.

A



B

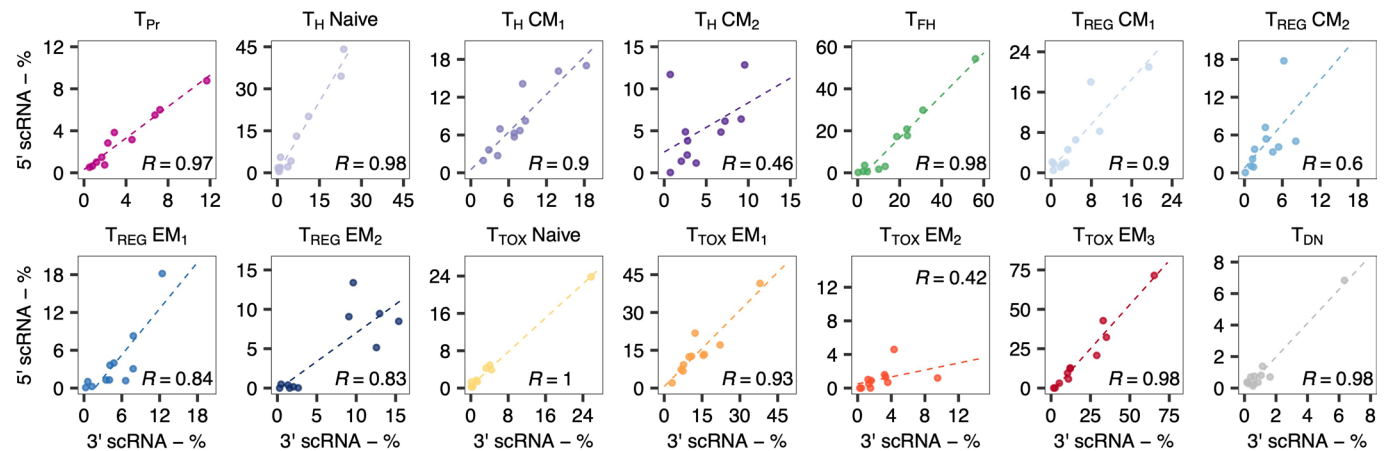


Extended Data Fig. 4 | Multinomial and multivariate models to explain varying T-cell subset proportions. **a)** Beta coefficients derived from a LASSO-regularized multinomial regression model predicting rLN, MZL, FL, MCL, or DLBCL based on the subset and overall T-cell proportions. **b)** Multivariate linear models were fit using sex, age, treatment status, COO (only DLBCL) as covariates, and the proportion of each T-cell subset as dependent variable in a two-sided fashion. Models were fit for the total dataset and for each entity separately, as

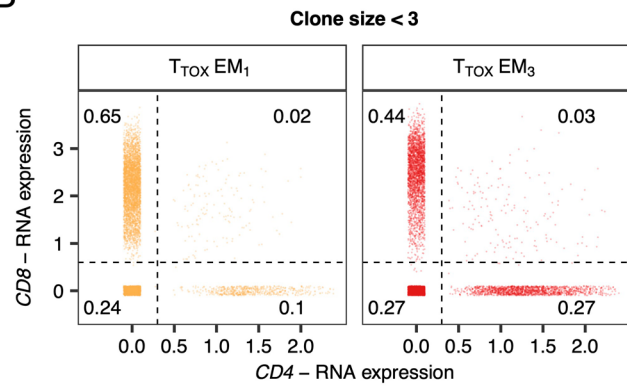
indicated. Diameter and color of the dots indicate $-\log_{10} p$ value and size of the coefficient, respectively. P values were corrected using the Benjamini-Hochberg procedure and significant p values are indicated by +/-.

A-B) Analysis is based on $n=101$ biologically independent samples. T_{Pr} : Proliferating T-cells. T_H : Helper T-cells. T_{FH} : Follicular helper T-cells. T_{REG} : Regulatory T-cells. T_{TOX} : Cytotoxic T-cells. T_{DN} : Double negative T-cells. CM: Central memory. EM: Effector memory. COO: Cell-of-origin.

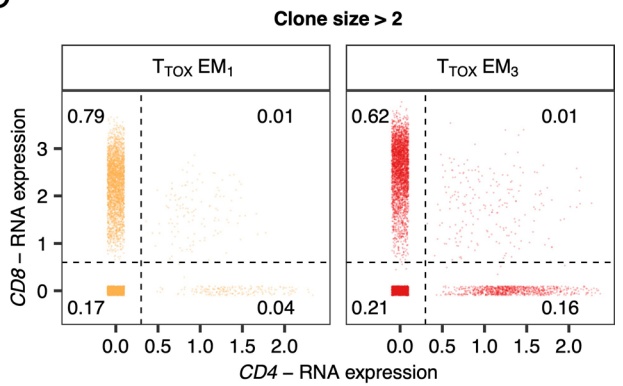
A



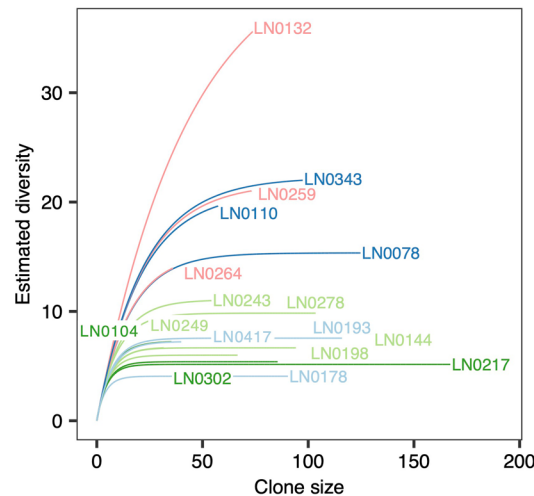
B



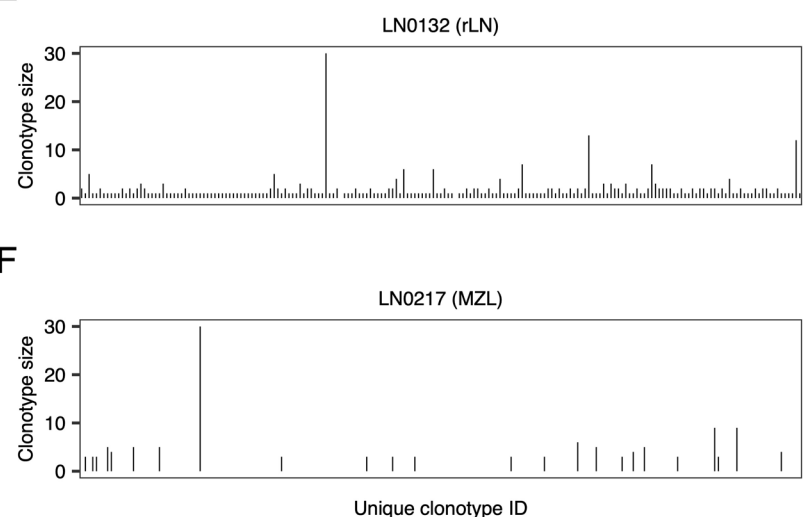
C



D

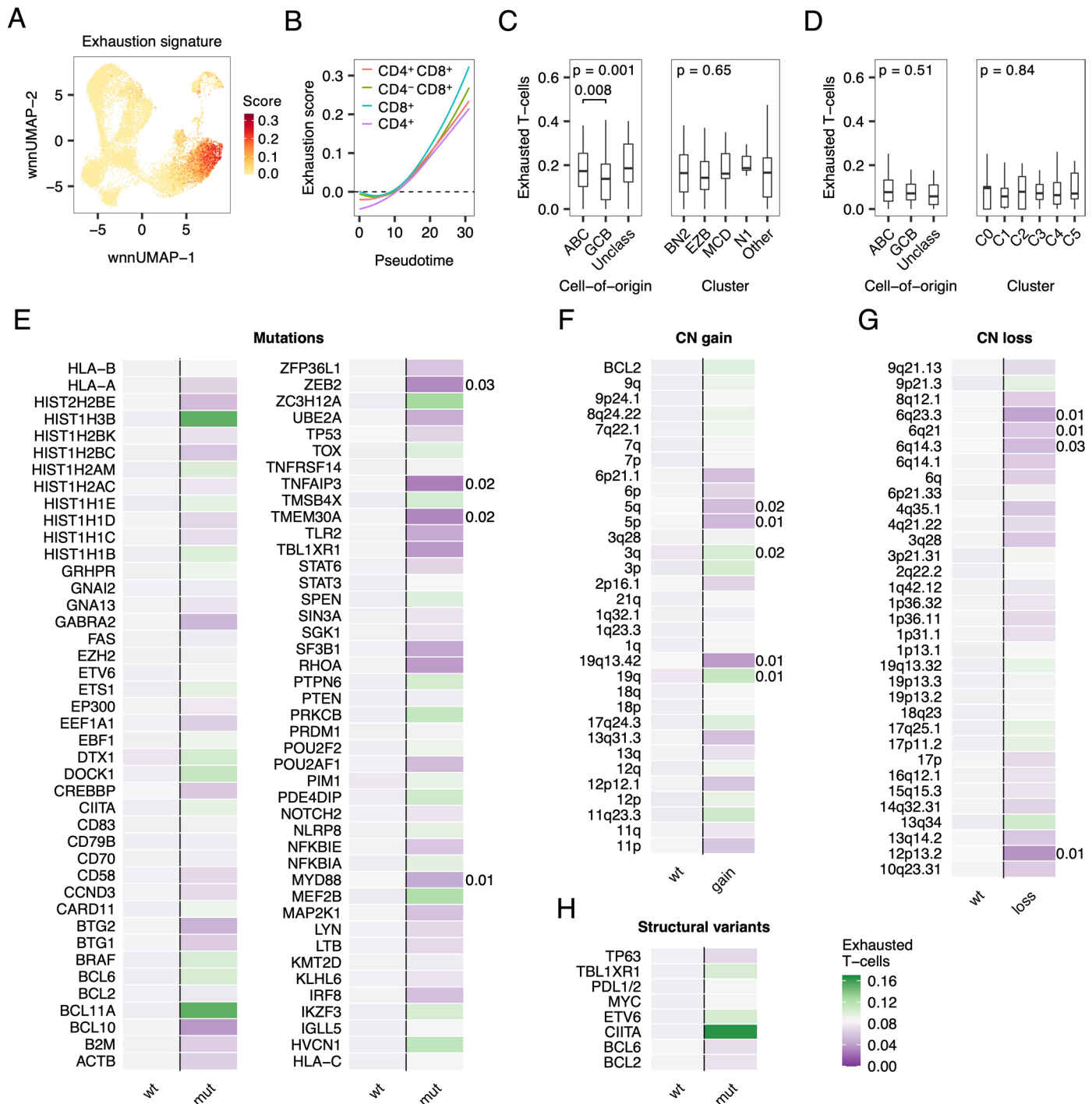


E



Extended Data Fig. 5 | 5' scRNA alongside full-length TCR sequencing and TCR diversity. 5' scRNA alongside full-length TCR repertoire data from $n = 17$ biologically independent lymph node samples were mapped to the CITE-seq reference data. **a**) T-cell subset proportions determined by 5' scRNA or CITE-seq reference data were correlated across 17 patient samples and 14 multimodally defined T-cell subsets. R values represent Pearson's linear correlation coefficients. **b-c)** CD4 and CD8 gene expression of T_{TOX} EM₁ and T_{TOX} EM₃ cells with clone size smaller (B) or greater / equal 3 (C). Dots are jittered in x and y direction.

Numbers indicate proportions of CD4⁺, CD8⁺, CD4⁺ CD8[−], or CD4[−] CD8[−] T-cells. **d**) TCR diversity was estimated for each LN patient sample using a rarefaction analysis (D). **e-f)** TCR diversity is exemplarily illustrated showing the 10 % most abundant clonotypes per sample. T_{Pr} : Proliferating T-cells. T_H : Helper T-cells. T_{FH} : Follicular helper T-cells. T_{REG} : Regulatory T-cells. T_{TOX} : Cytotoxic T-cells. T_{DN} : Double negative T-cells. CM: Central memory. EM: Effector memory. TCR: T-cell receptor.

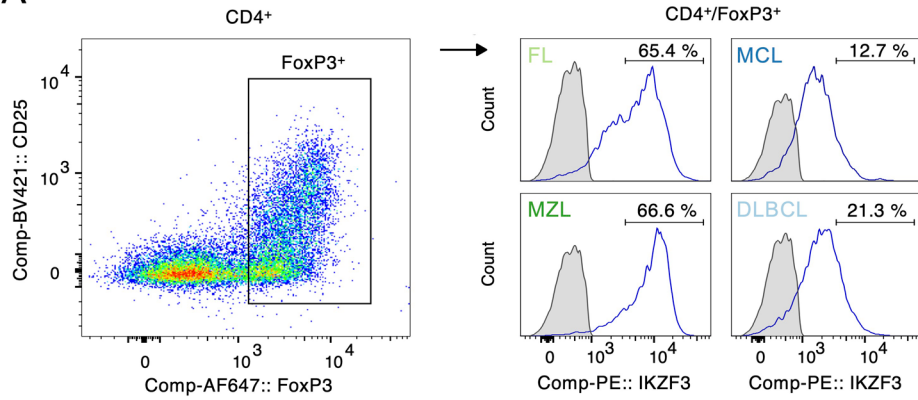


Extended Data Fig. 6 | T-cell exhaustion associated with genetic features.

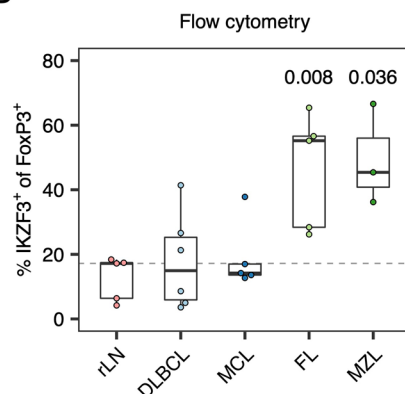
a) An exhaustion score was calculated based on a transcriptional signature of terminally exhausted T-cells (see Method section for details) and then projected onto the reference UMAP plot. **b**) Locally estimated scatterplot smoothing (loess) of pseudotime versus exhaustion score (as shown in panel A) separately for CD4+, CD8+, CD4+CD8+, and CD4-CD8- T_{TOX} cells. **c-h**) Bulk RNA-seq data from DLBCL patients from the Schmitz et al. cohort (C, n = 190) or the Chapuy et al. cohort (D-H, n = 137) were deconvoluted based on a gene expression signature of terminally exhausted T-cells. Box plots (C-D) show associations between T-cell exhaustion and cell-of-origin or genetic subtypes. Conditions were tested for significance using the Kruskal-Wallis-test. Wilcoxon-test was used as post-hoc

test (C). Heatmaps (E-H) illustrate the mean estimated proportion of exhausted T-cells for somatic variants (E), amplifications (F), deletions (G), or structural variants (H), as indicated, based on deconvolution of the bulk RNA-seq of the Chapuy et al. cohort (n = 137). Conditions were tested for significance using the two-sided Wilcoxon-test and corrected for multiple testing using the Benjamini-Hochberg procedure. After correction, all p values were > 0.05. To highlight the strongest differences, uncorrected p values ≤ 0.05 are shown to the right of each panel. Box plots: centre line, median; box limits, first and third quartile; whiskers, 1.5 x interquartile range. ABC: Activated B-cell subtype. GCB: Germinal center B-cell subtype. CN: Copy number.

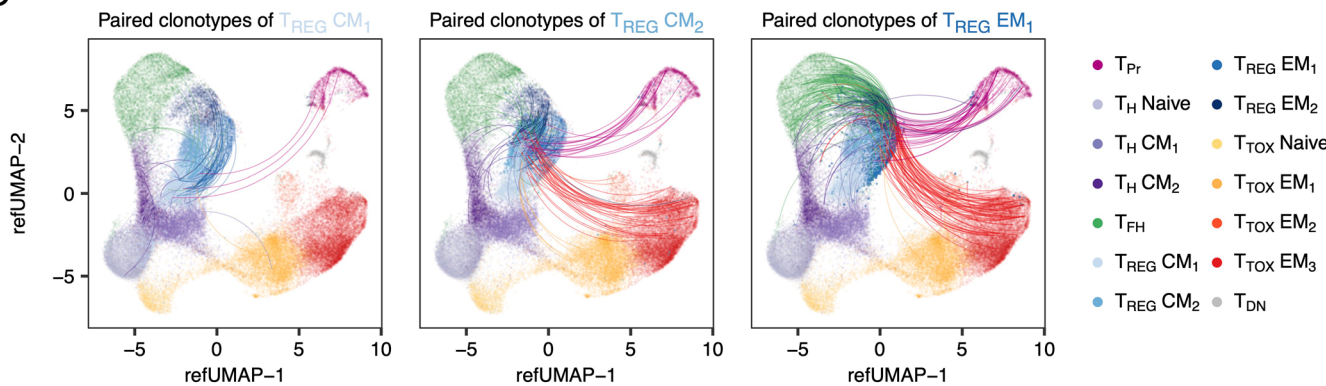
A



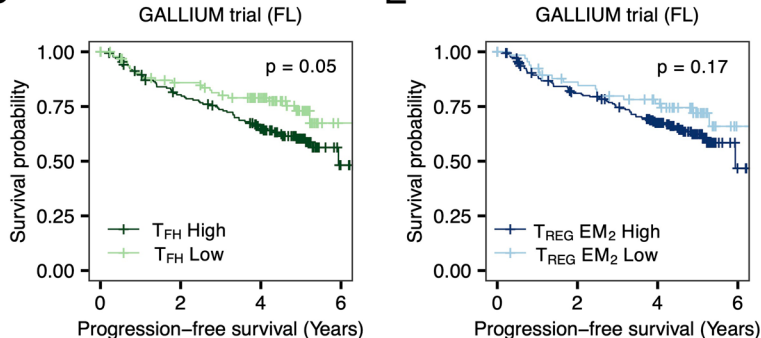
B



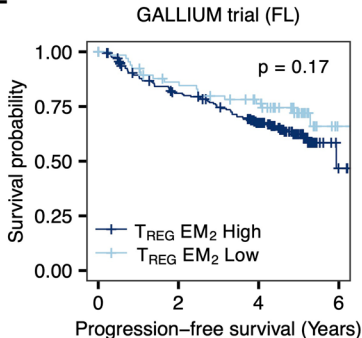
C



D

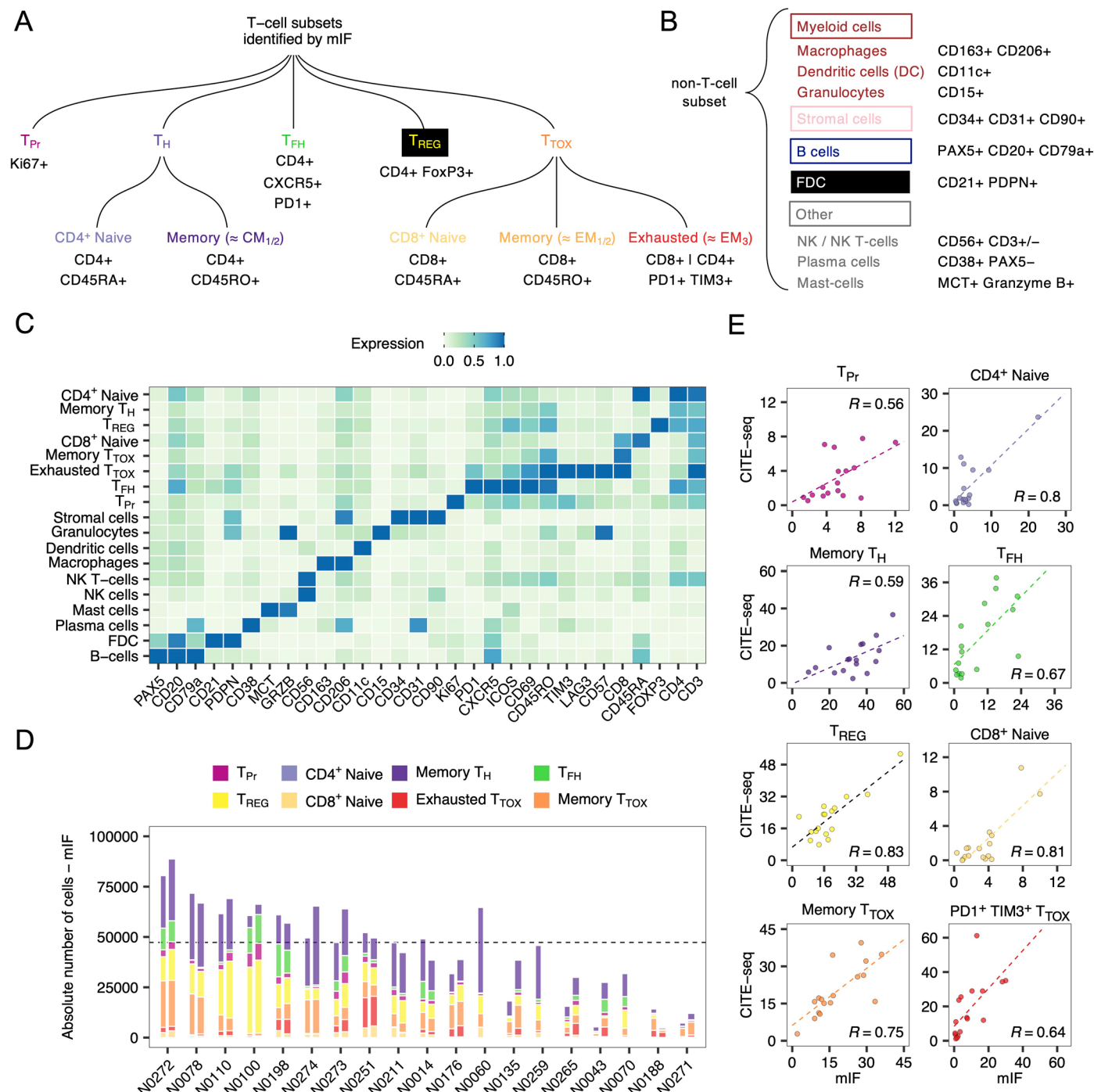


E



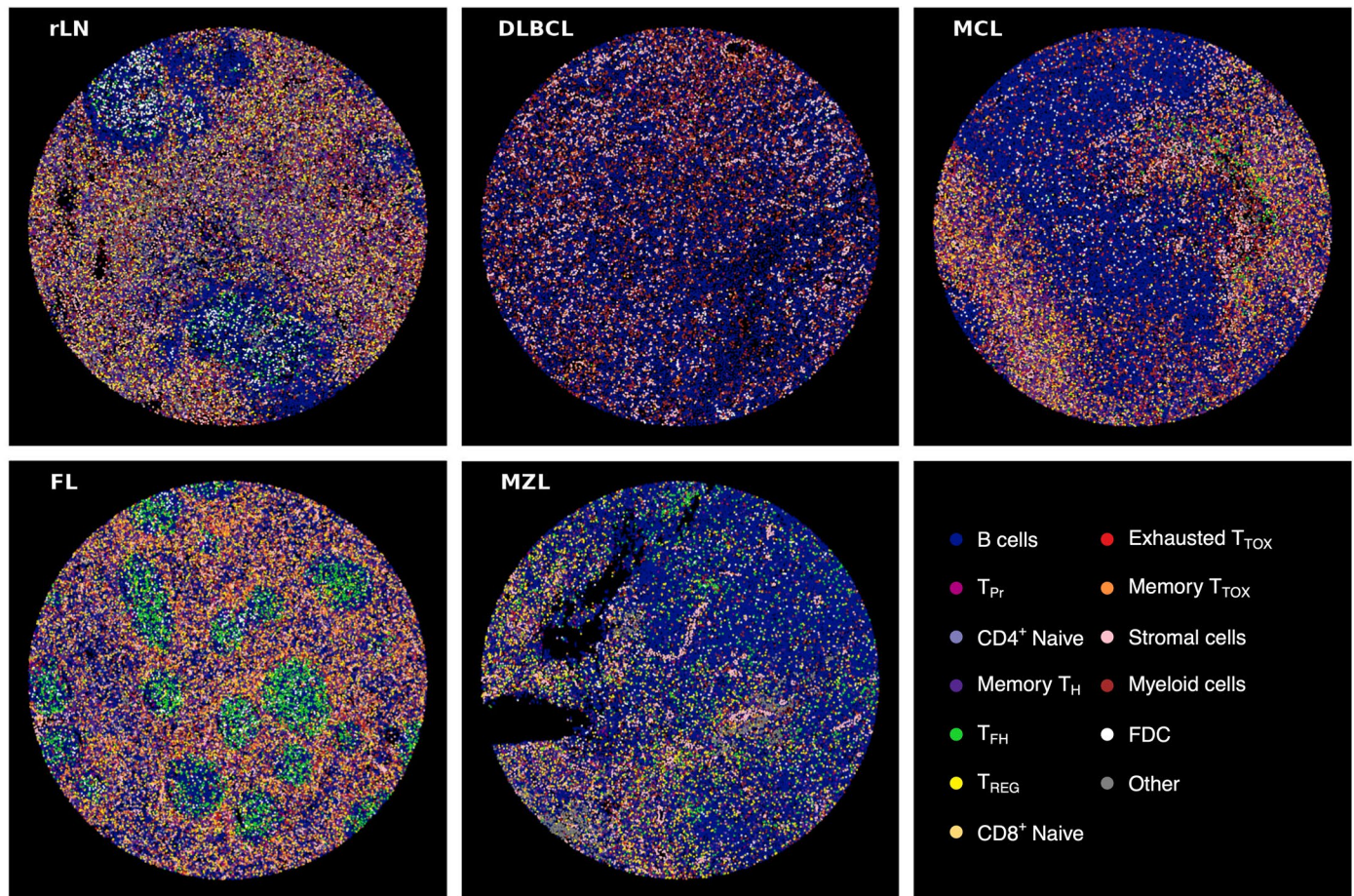
Extended Data Fig. 7 | T_{REG} EM₂ express IKZF3 at protein level and have no impact on overall survival in FL. **a**) Representative pseudocolor and density plots showing the IKZF3 (Aiolos) protein expression in CD4⁺ FoxP3⁺ cells determined by flow cytometry. Numbers indicate percentage of positive cells based on gates as indicated. Grey shaded histogram represent fluorescence-minus-one control. **b**) IKZF3 protein expression in FoxP3⁺ T-cells determined by flow cytometry in $n = 24$ biologically independent B-cell lymphoma patient samples. Each entity was tested versus tumour-free samples (rLN) using the two-sided Wilcoxon-test. Only p values ≤ 0.05 are shown. **c**) 5' scRNA alongside full-length TCR repertoire data from 11 biologically independent samples were

mapped to the CITE-seq reference data. Lines connect all T_{REG} CM₁, T_{REG} CM₂ or T_{REG} EM₁ cells with any other cell given that both T-cells have the same TCR clonotype. **d-e**) Bulk RNA-seq data from patients with FL were deconvoluted based on gene expression signature of T_{REG} EM₂ (D) or T_{FH} cells (E). Kaplan-Meier plots with p values of corresponding log-rank test. Box plots: centre line, median; box limits, first and third quartile; whiskers, 1.5x interquartile range. TCR: T-cell receptor. T_{Pr} : Proliferating T-cells. T_H : Helper T-cells. T_{FH} : Follicular helper T-cells. T_{REG} : Regulatory T-cells. T_{TOX} : Cytotoxic T-cells. T_{DN} : Double negative T-cells. CM: Central memory. EM: Effector memory.



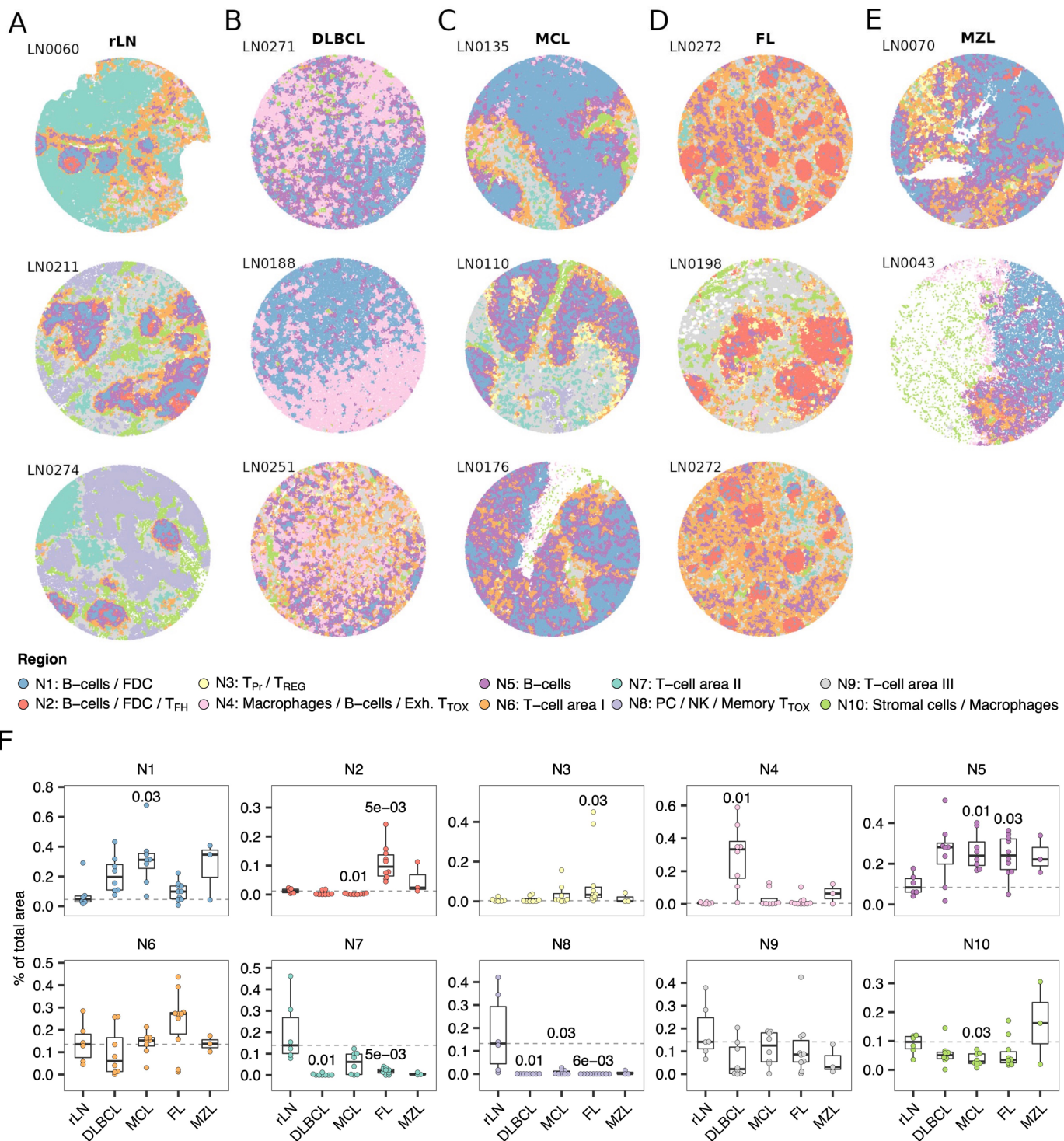
Extended Data Fig. 8 | Profiles of cell types and T-cell subpopulations identified by multiplexed immunofluorescence. **a-b)** Overview of T-cell subsets (A) and other cell types (B) identified by highly multiplexed immunofluorescence including their marker profiles. **c)** Heatmap illustrating the mean expression of key marker proteins that were used to annotate the 18 cell types and T-cell subsets using highly multiplexed immunofluorescence. Expression values were scaled between 0 and 1. **d)** Shown are the absolute numbers of T-cells per subset, tissue core, and patient. A maximum number of two cores per patient were imaged. **e)** The low-granularity T-cell

subpopulations detected by multiplexed immunofluorescence were aligned with the 14 high-granularity T-cell subsets identified by CITE-seq. Shown is the correlation of proportions for each of the T-cell subpopulations across $n = 19$ biologically independent LN samples that were analyzed by both approaches. Pearson's correlation coefficient is given for each panel (R). mIF: Multiplexed immunofluorescence. T_{Pr}: Proliferating T-cells. T_H: Helper T-cells. T_{FH}: Follicular helper T-cells. T_{REG}: Regulatory T-cells. T_{TOX}: Cytotoxic T-cells. CM: Central memory. EM: Effector memory. FDC: Follicular dendritic cells.



Extended Data Fig. 9 | Representative lymph node tissue cores colored by T-cell subpopulation or non T-cell cell types. Shown are five representative LN tissue cores for all entities investigated. Each cell was colored by T-cell subsets or

non T-cell cell types as indicated. FDC: Follicular dendritic cell. T_{Pr} : Proliferating T-cells. T_H : Helper T-cells. T_{FH} : Follicular helper T-cells. T_{REG} : Regulatory T-cells. T_{TOX} : Cytotoxic T-cells. FDC: Follicular dendritic cells.



Extended Data Fig. 10 | Qualitative and quantitative patterns of cellular neighbourhoods. **a–e**) Representative lymph node-derived tissue cores from three or two different patients per entity. Each cell was colored according to its neighbourhood. **F**) Box plots showing the proportions of selected neighborhoods of each tissue core across $n = 19$ biologically independent samples. Each entity and neighborhood was tested versus rLN using the two-sided

Wilcoxon-test. P values were corrected for multiple testing using the Benjamini-Hochberg procedure. Only $p \leq 0.05$ are shown. Dashed lines indicate the median of rLN. Box plots: centre line, median; box limits, first and third quartile; whiskers, $1.5 \times$ interquartile range. rLN: Tumor-free lymph node. T_{Pr}: Proliferating T-cells. T_{FH}: Follicular helper T-cells. T_{REG}: Regulatory T-cells. T_{TOX}: Cytotoxic T-cells. FDC: Follicular dendritic cells.

Reporting Summary

Nature Portfolio wishes to improve the reproducibility of the work that we publish. This form provides structure for consistency and transparency in reporting. For further information on Nature Portfolio policies, see our [Editorial Policies](#) and the [Editorial Policy Checklist](#).

Statistics

For all statistical analyses, confirm that the following items are present in the figure legend, table legend, main text, or Methods section.

n/a Confirmed

- The exact sample size (n) for each experimental group/condition, given as a discrete number and unit of measurement
- A statement on whether measurements were taken from distinct samples or whether the same sample was measured repeatedly
- The statistical test(s) used AND whether they are one- or two-sided
Only common tests should be described solely by name; describe more complex techniques in the Methods section.
- A description of all covariates tested
- A description of any assumptions or corrections, such as tests of normality and adjustment for multiple comparisons
- A full description of the statistical parameters including central tendency (e.g. means) or other basic estimates (e.g. regression coefficient) AND variation (e.g. standard deviation) or associated estimates of uncertainty (e.g. confidence intervals)
- For null hypothesis testing, the test statistic (e.g. F , t , r) with confidence intervals, effect sizes, degrees of freedom and P value noted
Give P values as exact values whenever suitable.
- For Bayesian analysis, information on the choice of priors and Markov chain Monte Carlo settings
- For hierarchical and complex designs, identification of the appropriate level for tests and full reporting of outcomes
- Estimates of effect sizes (e.g. Cohen's d , Pearson's r), indicating how they were calculated

Our web collection on [statistics for biologists](#) contains articles on many of the points above.

Software and code

Policy information about [availability of computer code](#)

Data collection

Flow cytometry data were collected using FACSDiva (version 8, BD Biosciences).
Multiplexed immunofluorescence data were recorded using CODEX driver software (version 1.29.0.1, Akoya Biosciences).
Raw TIFF images were processed using the RAPID pipeline in Matlab (version R2020a).
Single cell data were processed using CellRanger pipelines (10x Genomics, version 6.1.1).

Data analysis

FlowJo (v10.8.0).
ImageJ/Fiji (v1.53q).
Scanpy (v1.8.2)
Cellseg (v2022)
R (v4.2.1)
The computational codes, in the form of Rmarkdown documents, for reproducing all main and supplementary figures is available on GitHub (github.com/Huber-group-EMBL/CITEseqLN-Tcells.git). This contains also all R packages including version numbers used for data analysis.
R packages
knitr (v1.40)
glmnet (v4.1-2)
ggplotify (v0.1.0)
maxstat (v0.7-25)
R.oo (v1.24.0)
rstatix (v0.7.0)
viridis (v0.6.2)
dplyr (v1.0.10)

```

tidyverse (v1.3.1)
FNN (v1.1.3)
Matrix (v1.5-1)
ggraph (v2.0.6)
survival (v3.2-13)
R.methodsS3 (v1.8.1)
ggpubr (v0.4.0)
viridisLite (v0.4.1)
purrr (v0.3.4)
future.apply (v1.8.1)
immunarch (v0.7.0)
igraph (v1.3.5)
survminer (v0.4.9)
readxl (v1.4.1)
ggrepel (v0.9.1)
SeuratObject (v4.0.4)
readr (v2.1.2)
future (v1.23.0)
data.table (v1.14.2)
ggrastr (v1.0.1)
ggridges (v0.5.3)
caret (v6.0-90)
matrixStats (v0.61.0)
Seurat (v4.1.0)
tidyR (v1.2.1)
pamr (v1.56.1)
dplyr (v1.2.2)
ggtext (v0.1.1)
cowplot (v1.1.1)
lattice (v0.20-45)
scales (v1.2.1)
forcats (v0.5.1)
tibble (v3.1.8)
cluster (v2.1.2)
rmdformats (v1.0.4)
ggalluvial (v0.12.3)
R.utils (v2.11.0)
patchwork (v1.1.2)
RColorBrewer (v1.1-3)
stringr (v1.4.1)
ggplot2 (v3.3.6)

```

For manuscripts utilizing custom algorithms or software that are central to the research but not yet described in published literature, software must be made available to editors and reviewers. We strongly encourage code deposition in a community repository (e.g. GitHub). See the Nature Portfolio [guidelines for submitting code & software](#) for further information.

Data

Policy information about [availability of data](#)

All manuscripts must include a [data availability statement](#). This statement should provide the following information, where applicable:

- Accession codes, unique identifiers, or web links for publicly available datasets
- A description of any restrictions on data availability
- For clinical datasets or third party data, please ensure that the statement adheres to our [policy](#)

RNA-seq, epitope and TCR data that support the findings of this study have been deposited in the Gene Expression Omnibus (GEO) under accession codes GSE252608 and GSE252455. Highly multiplexed immunofluorescence images will be available in the BioStudies database (<https://www.ebi.ac.uk/biostudies/>) under accession number S-BIAD565 [88]. Flow cytometry data have been deposited in figshare under 10.6084/m9.figshare.24915633.

Human research participants

Policy information about [studies involving human research participants and Sex and Gender in Research](#).

Reporting on sex and gender

None of our findings was specific to only one sex. A total number of 55 male and 46 female lymph node samples were investigated in this study. Sex was collected from patient charts and irrelevant for sample collection. Informed consent to collect sex as meta data was given in advance. Sex was investigated as covariate for T-cell subset abundance. No significant association with sex were detected.

Population characteristics

The patient characteristics which are relevant for this study are listed in detail in Supplementary Table 1.

Recruitment

Patient samples were selected based on the diagnosis (diffuse large B cell lymphoma, follicular lymphoma, marginal zone lymphoma, mantle cell lymphoma, reactive lymphadenitis) and the availability of high quality viable cells in our lymph node biobank. There is no self-selection bias or other biases in recruitment.

Note that full information on the approval of the study protocol must also be provided in the manuscript.

Field-specific reporting

Please select the one below that is the best fit for your research. If you are not sure, read the appropriate sections before making your selection.

Life sciences Behavioural & social sciences Ecological, evolutionary & environmental sciences

For a reference copy of the document with all sections, see nature.com/documents/nr-reporting-summary-flat.pdf

Life sciences study design

All studies must disclose on these points even when the disclosure is negative.

Sample size	No statistical method was used to determine sample size prior to data collection. To estimate sufficient sample size, we performed an extensive literature research. We aimed for a sample size that exceeds 9 out of 10 studies using similar technical approaches on human samples as we used. The result was a sample size of around 10 samples per group / entity, i.e. 50 samples in total. Our core analysis about the quantitative infiltration patterns is even based on 100 samples. Further, in-depth experiments were performed on a subset of samples in order to confirm null hypothesis.
Data exclusions	No data were excluded from the analysis.
Replication	All experiments were independently replicated to verify reproducibility. The number of biological replicates is given for each figure.
Randomization	Not relevant. We do not have any experimental groups in our study.
Blinding	Not relevant. We do not have any experimental groups in our study.

Reporting for specific materials, systems and methods

We require information from authors about some types of materials, experimental systems and methods used in many studies. Here, indicate whether each material, system or method listed is relevant to your study. If you are not sure if a list item applies to your research, read the appropriate section before selecting a response.

Materials & experimental systems		Methods	
n/a	Involved in the study	n/a	Involved in the study
<input type="checkbox"/>	<input checked="" type="checkbox"/> Antibodies	<input type="checkbox"/>	<input type="checkbox"/> ChIP-seq
<input checked="" type="checkbox"/>	<input type="checkbox"/> Eukaryotic cell lines	<input type="checkbox"/>	<input checked="" type="checkbox"/> Flow cytometry
<input checked="" type="checkbox"/>	<input type="checkbox"/> Palaeontology and archaeology	<input type="checkbox"/>	<input type="checkbox"/> MRI-based neuroimaging
<input checked="" type="checkbox"/>	<input type="checkbox"/> Animals and other organisms		
<input checked="" type="checkbox"/>	<input type="checkbox"/> Clinical data		
<input checked="" type="checkbox"/>	<input type="checkbox"/> Dual use research of concern		

Antibodies

Antibodies used

CITE-seq
 Target, Gene, Clone, Isotype, Supplier, Catalogue, Barcode No, Barcode, Dilution
 CD10, MME, H10a, Mouse IgG1 κ, Biolegend, 312231, 0062, CAGCCATTCTATTAGG, 1:4
 CD103, ITGAE, Ber- ACT8, Mouse IgG1 κ, Biolegend, 350231, 0145, GACCTATTGTGAAT, 1:32
 CD11b, ITGAM, ICRF44, Mouse IgG1 κ, Biolegend, 301353, 0161, GACAAGTGATCTGCA, 1:10
 CD11c, ITGAX, S-HCL-3, Mouse IgG2b κ, Biolegend, 371519, 0053, TACGCCTATAACTTG, 1:16
 CD127, IL7R, A019D5, Mouse IgG1 κ, Biolegend, 351352, 0390, GTGTGTTGCTCTATG, 1:8
 CD134, TNFRSF4, Ber- ACT35, Mouse IgG1 κ, Biolegend, 350033, 0158, AACCCACCGTTGTTA, 1:4
 CD137, TNFRSF9, 4B4-1, Mouse IgG1 κ, Biolegend, 309835, 0355, CAGTAAGTTCGGGAC, 1:4
 CD150, SLAMF1, A12 (7D4), Mouse IgG1 κ, Biolegend, 306313, 0870, GTCATTTGATGTCTG, 1:4
 CD152, CTLA4, BNI3, Mouse IgG2a κ, Biolegend, 369619, 0151, ATGGTTCACGTAATC, 1:4
 CD16, FCGR3A, 3G8, Mouse IgG1 κ, Biolegend, 302061, 0083, AAGTTCACTCTTGC, 1:8
 CD161, KLRB1, HP-3G10, Mouse IgG1 κ, Biolegend, 339945, 0149, GTACGCAGTCCTTCT, 1:4
 CD183, CXCR3, G025H7, Mouse IgG1 κ, Biolegend, 353745, 0140, GCGATGGTAGATTAT, 1:8
 CD184, CXCR4, 12G5, Mouse IgG2a κ, Biolegend, 306531, 0366, TCAGGTCTTCAAC, 1:2
 CD185, CXCR5, J252D4, Mouse IgG1 κ, Biolegend, 356937, 0144, AATTCACCGTCGCC, 1:4
 CD19, CD19, HIB19, Mouse IgG1 κ, Biolegend, 302259, 0050, CTGGGCAATTACTCG, 1:16

CD194,CCR4,L291H4,Mouse IgG1 κ,Biolegend,359423,0071,AGCTTACCTGCACGA,1:16
 CD195,CCR5,J418F1,Rat IgG2b κ,Biolegend,359135,0141,CCAAAGTAAGAGCCA,1:4
 CD197,CCR7,G043H7,Mouse IgG2a κ,Biolegend,353247,0148,AGTCAGTCACCGA,1:1.25
 CD2,CD2,TS1/8,Mouse IgG1 κ,Biolegend,309229,0367,TACGATTGTCAGGG,1:16
 CD20,MS4A1,2H7,Mouse IgG2b κ,Biolegend,302359,0100,TTCTGGTCCCTAGA,1:8
 CD21,CR2,Bu32,Mouse IgG1 κ,Biolegend,354915,0181,AACCTAGTAGTTGG,1:16
 CD22,CD22,S-HCL-1,Mouse IgG2b κ,Biolegend,363514,0393,GGGTTGTTGTCITTG,1:16
 CD223,LAG3,11C3C65,Mouse IgG1 κ,Biolegend,369333,0152,CATTGGTCTGCCGGT,1:4
 CD23,FCER2,EBVCS-5,Mouse IgG1 κ,Biolegend,338523,0897,TCTGTATAACCGTCT,1:4
 CD24,CD24,ML5,Mouse IgG2a κ,Biolegend,311137,0180,AGATTCTTCGTGTT,1:4
 CD244,CD244,C1.7,Mouse IgG1 κ,Biolegend,329527,0189,TCGCTGGATGGTAG,1:16
 CD25,IL2RA,BC96,Mouse IgG1 κ,Biolegend,302643,0085,TTTGTCTGTACGCC,1:8
 CD27,CD27,O323,Mouse IgG1 κ,Biolegend,302847,0154,GCACCTCTGCATGTA,1:8
 CD273,PDCD1LG2,24F.10C12,Mouse IgG2a κ,Biolegend,329619,0008,TCAACGCTTGGCTAG,1:8
 CD274,PDCD1LG1,29E.2A3,Mouse IgG2b κ,Biolegend,329743,0007,GTTGTCGACAATAC,1:4
 CD278,ICOS,C398.4A,Armenian Hamster IgG,Biolegend,313555,0171,CGCGCACCCATTAAA,1:4
 CD279,PDCD1,EH12.2H7,Mouse IgG1 κ,Biolegend,329955,0088,ACAGCGCGTATTTA,1:8
 CD28,CD28,CD28.2,Mouse IgG1 κ,Biolegend,302955,0386,TGAGAACGACCCCTAA,1:4
 CD29,ITGB1,TS2/16,Mouse IgG1 κ,Biolegend,303027,0369,GTATTCCTCAGTCA,1:8
 CD3,CD3E,UCHT1,Mouse IgG1 κ,Biolegend,300475,0034,CTCATTGTAACCTCCT,1:8
 CD31,PECAM1,WM59,Mouse IgG1 κ,Biolegend,303137,0124,ACCTTATGCCACGG,1:8
 CD32,FCGR2A,FUN-2,Mouse IgG2b κ,Biolegend,303223,0142,GCTTCCGAATTACCG,1:16
 CD357,TNFRSF18,108-17,Mouse IgG2a κ,Biolegend,371225,0360,ACCTTCGACACTCG,1:4
 CD366,HAVCR2,F38-2E2,Mouse IgG1 κ,Biolegend,345047,0169,TGTCTTACCCAACCTT,1:4
 CD38,CD38,HIT2,Mouse IgG1 κ,Biolegend,303541,0389,TGTACCCGCTTGTGA,1:8
 CD39,ENTPD1,A1,Mouse IgG1 κ,Biolegend,328233,0176,TTACCTGGTATCCGT,1:16
 CD4,CD4,RPA-T4,Mouse IgG1 κ,Biolegend,300563,0072,TGTTCCCGCTCACT,1:8
 CD43,SPN,CD43-10G7,Mouse IgG1 κ,Biolegend,343209,0357,GATTAACCAAGCTCAT,1:4
 CD44,CD44,IM7,Rat IgG2b κ,Biolegend,103045,0073,TGGCTTCAGGTCTTA,1:6
 CD45,PTPRC,HI30,Mouse IgG1 κ,Biolegend,304064,0391,TGCAATTACCCGGAT,1:40
 CD45RA,PTPRC,HI100,Mouse IgG2b κ,Biolegend,304157,0063,TCAATCCTCCGCTT,1:40
 CD45RO,PTPRC,UCHL1,Mouse IgG2a κ,Biolegend,304255,0087,CTCGAATCATGTTG,1:10
 CD47,CD47,CC2C6,Mouse IgG1 κ,Biolegend,323129,0026,GCATTCTGTACCTA,1:10
 CD48,CD48,BJ40,Mouse IgG1 κ,Biolegend,336709,0029,CTACGACGTAGAAGA,1:8
 CD5,CD5,UCHT2,Mouse IgG1 κ,Biolegend,300635,0138,CATTAACGGGATGCC,1:16
 CD56,NCAM1,QA17A16,Mouse IgG1 κ,Biolegend,392421,0084,TTGCCGCATTGAGT,1:10
 CD57,B3GAT1,QA17A04,Mouse IgG1 κ,Biolegend,393319,0168,AACTCCCTATGGAGG,1:4
 CD62L,SELL,DREG-56,Mouse IgG1 κ,Biolegend,304847,0147,GTCCCTGCAACTTGA,1:16
 CD69,CD69,FN50,Mouse IgG1 κ,Biolegend,310947,0146,GTCTCTGGCTTAAA,1:8
 CD7,CD7,CD7-6B7,Mouse IgG2a κ,Biolegend,343123,0066,TGGATTCCCGGACTT,1:16
 CD70,CD70,113-16,Mouse IgG1 κ,Biolegend,355117,0027,CGCGAACATAAGAAG,1:4
 CD73,NT5E,AD2,Mouse IgG1 κ,Biolegend,344029,0577,CAGTTCCCTAGTTG,1:4
 CD79b,CD79B,CB3-1,Mouse IgG1 κ,Biolegend,341415,0187,ATTCTCAACCGAAG,1:8
 CD86,CD86,IT2.2,Mouse IgG2b κ,Biolegend,305443,0006,GTCTTGTAGTGCA,1:16
 CD8a,CD8A,RPA-T8,Mouse IgG1 κ,Biolegend,301067,0080,GCTGCGCTTCCATT,1:8
 CD95,FAS,DX2,Mouse IgG1 κ,Biolegend,305649,0156,CCAGCTCATTAGAGC,1:8
 Isotype Ctrl.,MOPC-21,Mouse IgG1 κ,Biolegend,400199,0090,GCCGGACGACATTA,1:4
 Isotype Ctrl.,HTK888,Armenian Hamster IgG,Biolegend,400973,0241,CCTGTCATTAAGACT,1:8
 Isotype Ctrl.,MPC-11,Mouse IgG2b κ,Biolegend,400373,0092,ATATGTATCACCGA,1:4
 Isotype Ctrl.,RTK4530,Rat IgG2b κ,Biolegend,400673,0095,GATTCTTGACGACCT,1:4
 Isotype Ctrl.,MOPC-173,Mouse IgG2a κ,Biolegend,400285,0091,CTCCTACCTAAACTG,1:8
 Kappa,IGKC,MHK-49,Mouse IgG1 κ,Biolegend,316531,0894,AGCTCAGCCAGTATG,1:10
 KLRG1,KLRG1,SA231A2,Mouse IgG2a κ,Biolegend,367721,0153,CTTATTCCTGCCCT,1:8
 Lambda,IGLC2,MHL-38,Mouse IgG2a κ,Biolegend,316627,0898,CAGCCAGTAAGTCAC,1:10
 TIGIT,TIGIT,A15153G,Mouse IgG2a κ,Biolegend,372725,0089,TTGCTTACCGCCAGA,1:16

Flow Cytometry

Target,Conjugate,Alternative,Clone,Isotype,Supplier,Catalogue,Dilution
 CD25,BV421,,BC96,Mouse IgG1 κ,Biolegend,302629,1:25
 CD278,BV605,ICOS,WM59,Mouse IgG1 κ,Biolegend,303121,1:50
 CD185,BV711,CXCR5,J252D4,Mouse IgG1 κ,Biolegend,356934,1:12.5
 Ki67,BV785,,B56,Mouse IgG1 κ, BD Biosciences,563756,1:50
 CD45RA,FITC,,HI100,Mouse IgG2b κ,Biolegend,304105,1:100
 CD3,PerCP-Cy5.5,,OKT3,Mouse IgG2a κ,Biolegend,317336,1:25
 IKZF3,PE,Aiolos,16D9C97,Mouse IgG1 κ,Biolegend,371103,1:25
 CD4,PE-Dazzle,,RPA-T4,Mouse IgG1 κ,Biolegend,300548,1:50
 CD279,PE-Cy7,PD1,EH12.2H7,Mouse IgG1 κ,Biolegend,329918,1:25
 FoxP3,AF647,,259D/C7,Mouse IgG1 κ, BD Biosciences,560889,1:10
 CD69,AF700,,FN50,Mouse IgG1 κ,Biolegend,310922,1:25
 CD8,APC-Cy7,,HIT3a,Mouse IgG1 κ,Biolegend,300926,1:25
 CD244,BV421,,C1.7,Mouse IgG1 κ,Biolegend,329531,1:25
 CD31,BV605,,WM59,Mouse IgG1 κ,Biolegend,303121,1:25
 CD366,BV711,TIM3,F38-2E2,Mouse IgG1 κ,Biolegend,345023,1:25

CODEX

Target,Clone,Supplier,Catalogue (conjugated),CODEX oligo,Dilution

BCL6, K112-91, BD Biosciences, 561520, 79, 1:25
 GATA3, L50-823, Cell Marque, custom conjugation, 2, 1:50
 CD185, D6L3C, Cell Signaling Technology, custom conjugation, 69, 1:100
 Tbet, D6N8B, Cell Signaling Technology, custom conjugation, 68, 1:100
 CD62L, B-8, Santa Cruz Biotechnology, custom conjugation, 38, 1:400
 FoxP3, 236A/E7, Invitrogen, 14-4777-82, 61, 1:100
 CD163, EDHu-1, Novus Biologicals, NB110-40686, 59, 1:50
 Ki67, B56, BD Biosciences, 556003, 6, 1:200
 CD366, polyclonal, Novus Biologicals, AF2365, 44, 1:100
 PAX5, D7H5X, Cell Signaling Technology, custom conjugation, 66, 1:200
 CD134, Ber-ACT35, Biolegend, 350002, 75, 1:100
 IL10, polyclonal, R&D Systems, AF-217-NA, 67, 1:100
 CD5, vC5/473 + CD5/54/F6, Novus Biologicals, NBP2-34583, 25, 1:50
 CD206, MM0820-48L31, Abcam, custom conjugation, 55, 1:200
 CD25, 4C9, Cell Marque, custom conjugation, 24, 1:200
 CD16, D1N9L, Cell Signaling Technology, custom conjugation, 60, 1:50
 CD152, BSB-88, BioSB, BSB 2885 (ASR), 30, 1:25
 CD79a, HM47, Biolegend, 333502, 46, 1:200
 CD57, HNK-1, Biolegend, 359602, 29, 1:50
 CD34, QBEnd/10, Novus Biologicals, NBP2-34713, 11, 1:50
 CXCL13, polyclonal, Novus, AF801, 41, 1:200
 CD21, SP186, Abcam, ab240987, 15, 1:100
 CD7, MRQ56, Cell Marque, custom conjugation, 63, 1:100
 Podoplanin, D2-40, Biolegend, 916606, 32, 1:200
 CD279, D4W2J, Cell Signaling Technology, custom conjugation, 23, 1:50
 HLA-DR, EPR3692, Abcam, ab209968, 65, 1:100
 CD223, D2G4O, Cell Signaling Technology, custom conjugation, 42, 1:25
 CD20, rIGEL/773, Novus Biologicals, NBP2-54591, 48, 1:200
 CD56, MRQ-42, Cell Marque, custom conjugation, 58, 1:100
 CD45RO, UCH-L1, Santa Cruz Biotechnology, custom conjugation, 5, 1:50
 CD278, D1K2T, Cell Signaling Technology, custom conjugation, 74, 1:200
 CD90, EPR3132, Abcam, ab181885, 57, 1:150
 CD4, EPR6855, Abcam, ab181724, 20, 1:100
 CD11c, EP1347Y, Abcam, ab216655, 49, 1:200
 CD3, MRQ-39, Cell Marque, custom conjugation, 33, 1:50
 CD68, KP-1, BioLegend, 916104, 62, 1:200
 CD69, EPR21814, Abcam, ab234512, 36, 1:500
 CD14, EPR3653, Abcam, ab226121, 7, 1:300
 CD8, C8/144B, Cell Marque, custom conjugation, 8, 1:100
 Kappa light chain, L1C1, Cell Marque, custom conjugation, 70, 1:100
 CD45RA, HI100, Biolegend, 304102, 21, 1:200
 CD11b, EPR1344, Abcam, ab209970, 28, 1:200
 Granzyme B, EPR20129-217, Abcam, ab219803, 81, 1:200
 CD31, C31.3 + C31.10, Novus Biologicals, NBP2-47785, 51, 1:200
 CD45, 2B11+PD7/263, Novus Biologicals, NBP2-34528, 56, 1:200
 CD38, EPR4106, Abcam, ab176886, 3, 1:200
 CD44, IM7, Biolegend, 103002, 45, 1:200
 CD15, MMA, BD Biosciences, 559045, 14, 1:200
 Lambda light chain, Lamb14, Cell Marque, custom conjugation, 26, 1:200
 Mast cell tryptase, AA1, Abcam, ab2378, 71, 1:200

Validation

CITE-seq

Target, Gene, Clone, Validation

CD10, MME, HI10a, Commercial product, tested and titrated using the corresponding PE-conjugated antibody in flow cytometry (as recommended by the manufacturer) in peripheral blood mononuclear cells
 CD103, ITGAE, Ber-ACT8, Commercial product, tested and titrated using the corresponding PE-conjugated antibody in flow cytometry (as recommended by the manufacturer) in peripheral blood mononuclear cells
 CD11b, ITGAM, ICRF44, Commercial product, tested and titrated using the corresponding PE-conjugated antibody in flow cytometry (as recommended by the manufacturer) in peripheral blood mononuclear cells
 CD11c, ITGAX, S-HCL-3, Commercial product, tested and titrated using the corresponding PE-conjugated antibody in flow cytometry (as recommended by the manufacturer) in peripheral blood mononuclear cells
 CD127, IL7R, A019D5, Commercial product, tested and titrated using the corresponding PE-conjugated antibody in flow cytometry (as recommended by the manufacturer) in peripheral blood mononuclear cells
 CD134, TNFRSF4, Ber-ACT35, Commercial product, tested and titrated using the corresponding PE-conjugated antibody in flow cytometry (as recommended by the manufacturer) in peripheral blood mononuclear cells
 CD137, TNFRSF9, 4B4-1, Commercial product, tested and titrated using the corresponding PE-conjugated antibody in flow cytometry (as recommended by the manufacturer) in peripheral blood mononuclear cells
 CD150, SLAMF1, A12 (7D4), Commercial product, tested and titrated using the corresponding PE-conjugated antibody in flow cytometry (as recommended by the manufacturer) in peripheral blood mononuclear cells
 CD152, CTLA4, BNI3, Commercial product, tested and titrated using the corresponding PE-conjugated antibody in flow cytometry (as recommended by the manufacturer) in peripheral blood mononuclear cells
 CD16, FCGR3A, 3G8, Commercial product, tested and titrated using the corresponding PE-conjugated antibody in flow cytometry (as recommended by the manufacturer) in peripheral blood mononuclear cells
 CD161, KLRLB1, HP-3G10, Commercial product, tested and titrated using the corresponding PE-conjugated antibody in flow cytometry (as recommended by the manufacturer) in peripheral blood mononuclear cells
 CD183, CXCR3, G025H7, Commercial product, tested and titrated using the corresponding PE-conjugated antibody in flow cytometry

recommended by the manufacturer) in peripheral blood mononuclear cells
 CD56,NCAM1,QA17A16,Commercial product, tested and titrated using the corresponding PE-conjugated antibody in flow cytometry (as recommended by the manufacturer) in peripheral blood mononuclear cells
 CD57,B3GAT1,QA17A04,Commercial product, tested and titrated using the corresponding PE-conjugated antibody in flow cytometry (as recommended by the manufacturer) in peripheral blood mononuclear cells
 CD62L,SELL,DREG-56,Commercial product, tested and titrated using the corresponding PE-conjugated antibody in flow cytometry (as recommended by the manufacturer) in peripheral blood mononuclear cells
 CD69,CD69,FN50,Commercial product, tested and titrated using the corresponding PE-conjugated antibody in flow cytometry (as recommended by the manufacturer) in peripheral blood mononuclear cells
 CD7,CD7,CD7-6B7,Commercial product, tested and titrated using the corresponding PE-conjugated antibody in flow cytometry (as recommended by the manufacturer) in peripheral blood mononuclear cells
 CD70,CD70,113-16,Commercial product, tested and titrated using the corresponding PE-conjugated antibody in flow cytometry (as recommended by the manufacturer) in peripheral blood mononuclear cells
 CD73,NT5E,AD2,Commercial product, tested and titrated using the corresponding PE-conjugated antibody in flow cytometry (as recommended by the manufacturer) in peripheral blood mononuclear cells
 CD79b,CD79B,CB3-1,Commercial product, tested and titrated using the corresponding PE-conjugated antibody in flow cytometry (as recommended by the manufacturer) in peripheral blood mononuclear cells
 CD86,CD86,IT2.2,Commercial product, tested and titrated using the corresponding PE-conjugated antibody in flow cytometry (as recommended by the manufacturer) in peripheral blood mononuclear cells
 CD8a,CD8A,RPA-T8,Commercial product, tested and titrated using the corresponding PE-conjugated antibody in flow cytometry (as recommended by the manufacturer) in peripheral blood mononuclear cells
 CD95,FAS,DX2,Commercial product, tested and titrated using the corresponding PE-conjugated antibody in flow cytometry (as recommended by the manufacturer) in peripheral blood mononuclear cells
 Isotype Ctrl.,MOPC-21,Commercial product, tested and titrated using the corresponding PE-conjugated antibody in flow cytometry (as recommended by the manufacturer) in peripheral blood mononuclear cells
 Isotype Ctrl.,HTK888,Commercial product, tested and titrated using the corresponding PE-conjugated antibody in flow cytometry (as recommended by the manufacturer) in peripheral blood mononuclear cells
 Isotype Ctrl.,MPC-11,Commercial product, tested and titrated using the corresponding PE-conjugated antibody in flow cytometry (as recommended by the manufacturer) in peripheral blood mononuclear cells
 Isotype Ctrl.,RTK4530,Commercial product, tested and titrated using the corresponding PE-conjugated antibody in flow cytometry (as recommended by the manufacturer) in peripheral blood mononuclear cells
 Isotype Ctrl.,MOPC-173,Commercial product, tested and titrated using the corresponding PE-conjugated antibody in flow cytometry (as recommended by the manufacturer) in peripheral blood mononuclear cells
 Kappa,IGKC,MHK-49 ,Commercial product, tested and titrated using the corresponding PE-conjugated antibody in flow cytometry (as recommended by the manufacturer) in peripheral blood mononuclear cells
 KLRG1,KLRG1,SA231A2,Commercial product, tested and titrated using the corresponding PE-conjugated antibody in flow cytometry (as recommended by the manufacturer) in peripheral blood mononuclear cells
 Lambda,IGLC2,MHL-38 ,Commercial product, tested and titrated using the corresponding PE-conjugated antibody in flow cytometry (as recommended by the manufacturer) in peripheral blood mononuclear cells
 TIGIT,TIGIT,A15153G,Commercial product, tested and titrated using the corresponding PE-conjugated antibody in flow cytometry (as recommended by the manufacturer) in peripheral blood mononuclear cells

Flow Cytometry

Target,Conjugate,Clone,

CD25,BV421,BC96,Commercial product, routinely tested and extensively titrated in peripheral blood mononuclear cells
 CD278,BV605,WM59,Commercial product, routinely tested and extensively titrated in peripheral blood mononuclear cells
 CD185,BV711,J252D4,Commercial product, routinely tested and extensively titrated in peripheral blood mononuclear cells
 Ki67,BV785,B56,Commercial product, routinely tested and extensively titrated in peripheral blood mononuclear cells
 CD45RA,FITC,HI100,Commercial product, routinely tested and extensively titrated in peripheral blood mononuclear cells
 CD3,PerCP-Cy5.5,OKT3,Commercial product, routinely tested and extensively titrated in peripheral blood mononuclear cells
 IKZF3,PE,16D9C97,Commercial product, routinely tested and extensively titrated in peripheral blood mononuclear cells
 CD4,PE-Dazzle,RPA-T4,Commercial product, routinely tested and extensively titrated in peripheral blood mononuclear cells
 CD279,PE-Cy7,EH12.2H7,Commercial product, routinely tested and extensively titrated in peripheral blood mononuclear cells
 FoxP3,AF647,259D/C7,Commercial product, routinely tested and extensively titrated in peripheral blood mononuclear cells
 CD69,AF700,FN50,Commercial product, routinely tested and extensively titrated in peripheral blood mononuclear cells
 CD8,APC-Cy7,HIT3a,Commercial product, routinely tested and extensively titrated in peripheral blood mononuclear cells
 CD244,BV421,C1.7,Commercial product, routinely tested and extensively titrated in peripheral blood mononuclear cells
 CD31,BV605,WM59,Commercial product, routinely tested and extensively titrated in peripheral blood mononuclear cells
 CD366,BV711,F38-2E2,Commercial product, routinely tested and extensively titrated in peripheral blood mononuclear cells

CODEX

Target,Clone,CODEX oligo,Validation

BCL6,K112-91,79,Commercial product, extensive titration and validation in tonsils and tumor-free lymph nodes, reviewed by two independent board-certified hemato-pathologists
 GATA3,L50-823,2,Custom conjugation of commercially available unconjugated antibody, extensive titration and validation in tonsils and tumor-free lymph nodes, reviewed by two independent board-certified hemato-pathologists
 CD185,D6L3C,69,Custom conjugation of commercially available unconjugated antibody, extensive titration and validation in tonsils and tumor-free lymph nodes, reviewed by two independent board-certified hemato-pathologists
 Tbet,D6N8B,68,Custom conjugation of commercially available unconjugated antibody, extensive titration and validation in tonsils and tumor-free lymph nodes, reviewed by two independent board-certified hemato-pathologists
 CD62L,B-8,38,Custom conjugation of commercially available unconjugated antibody, extensive titration and validation in tonsils and tumor-free lymph nodes, reviewed by two independent board-certified hemato-pathologists
 FoxP3,236A/E7,61,Commercial product, extensive titration and validation in tonsils and tumor-free lymph nodes, reviewed by two independent board-certified hemato-pathologists
 CD163,EDHu-1,59,Commercial product, extensive titration and validation in tonsils and tumor-free lymph nodes, reviewed by two independent board-certified hemato-pathologists

Ki67,B56,6,Commercial product, extensive titration and validation in tonsils and tumor-free lymph nodes, reviewed by two independent board-certified hemato-pathologists

CD366,polyclonal,44,Commercial product, extensive titration and validation in tonsils and tumor-free lymph nodes, reviewed by two independent board-certified hemato-pathologists

PAX5,D7H5X,66,Custom conjugation of commercially available unconjugated antibody, extensive titration and validation in tonsils and tumor-free lymph nodes, reviewed by two independent board-certified hemato-pathologists

CD134,Ber-ACT35,75,Commercial product, extensive titration and validation in tonsils and tumor-free lymph nodes, reviewed by two independent board-certified hemato-pathologists

IL10,polyclonal,67,Commercial product, extensive titration and validation in tonsils and tumor-free lymph nodes, reviewed by two independent board-certified hemato-pathologists

CD5,vC5/473 + CD5/54/F6,25,Commercial product, extensive titration and validation in tonsils and tumor-free lymph nodes, reviewed by two independent board-certified hemato-pathologists

CD206,MM0820-48L31,55,Custom conjugation of commercially available unconjugated antibody, extensive titration and validation in tonsils and tumor-free lymph nodes, reviewed by two independent board-certified hemato-pathologists

CD25,4C9,24,Custom conjugation of commercially available unconjugated antibody, extensive titration and validation in tonsils and tumor-free lymph nodes, reviewed by two independent board-certified hemato-pathologists

CD16,D1N9L,60,Custom conjugation of commercially available unconjugated antibody, extensive titration and validation in tonsils and tumor-free lymph nodes, reviewed by two independent board-certified hemato-pathologists

CD152,BSB-88,30,Commercial product, extensive titration and validation in tonsils and tumor-free lymph nodes, reviewed by two independent board-certified hemato-pathologists

CD79a,HM47,46,Commercial product, extensive titration and validation in tonsils and tumor-free lymph nodes, reviewed by two independent board-certified hemato-pathologists

CD57,HNK-1,29,Commercial product, extensive titration and validation in tonsils and tumor-free lymph nodes, reviewed by two independent board-certified hemato-pathologists

CD34,QBEnd/10,11,Commercial product, extensive titration and validation in tonsils and tumor-free lymph nodes, reviewed by two independent board-certified hemato-pathologists

CXCL13,polyclonal,41,Commercial product, extensive titration and validation in tonsils and tumor-free lymph nodes, reviewed by two independent board-certified hemato-pathologists

CD21,SP186,15,Commercial product, extensive titration and validation in tonsils and tumor-free lymph nodes, reviewed by two independent board-certified hemato-pathologists

CD7,MRQ56,63,Custom conjugation of commercially available unconjugated antibody, extensive titration and validation in tonsils and tumor-free lymph nodes, reviewed by two independent board-certified hemato-pathologists

Podoplanin,D2-40,32,Commercial product, extensive titration and validation in tonsils and tumor-free lymph nodes, reviewed by two independent board-certified hemato-pathologists

CD279,D4W2J,23,Custom conjugation of commercially available unconjugated antibody, extensive titration and validation in tonsils and tumor-free lymph nodes, reviewed by two independent board-certified hemato-pathologists

HLA-DR,EPR3692,65,Commercial product, extensive titration and validation in tonsils and tumor-free lymph nodes, reviewed by two independent board-certified hemato-pathologists

CD223,D2G4O,42,Custom conjugation of commercially available unconjugated antibody, extensive titration and validation in tonsils and tumor-free lymph nodes, reviewed by two independent board-certified hemato-pathologists

CD20,rIGEL/773,48,Commercial product, extensive titration and validation in tonsils and tumor-free lymph nodes, reviewed by two independent board-certified hemato-pathologists

CD56,MRQ-42,58,Custom conjugation of commercially available unconjugated antibody, extensive titration and validation in tonsils and tumor-free lymph nodes, reviewed by two independent board-certified hemato-pathologists

CD45RO,UCH-L1,5,Custom conjugation of commercially available unconjugated antibody, extensive titration and validation in tonsils and tumor-free lymph nodes, reviewed by two independent board-certified hemato-pathologists

CD278,D1K2T,74,Custom conjugation of commercially available unconjugated antibody, extensive titration and validation in tonsils and tumor-free lymph nodes, reviewed by two independent board-certified hemato-pathologists

CD90,EPR3132,57,Commercial product, extensive titration and validation in tonsils and tumor-free lymph nodes, reviewed by two independent board-certified hemato-pathologists

CD4,EPR6855,20,Commercial product, extensive titration and validation in tonsils and tumor-free lymph nodes, reviewed by two independent board-certified hemato-pathologists

CD11c,EP1347Y,49,Commercial product, extensive titration and validation in tonsils and tumor-free lymph nodes, reviewed by two independent board-certified hemato-pathologists

CD3,MRQ-39,33,Custom conjugation of commercially available unconjugated antibody, extensive titration and validation in tonsils and tumor-free lymph nodes, reviewed by two independent board-certified hemato-pathologists

CD68,KP-1,62,Commercial product, extensive titration and validation in tonsils and tumor-free lymph nodes, reviewed by two independent board-certified hemato-pathologists

CD69,EPR21814,36,Commercial product, extensive titration and validation in tonsils and tumor-free lymph nodes, reviewed by two independent board-certified hemato-pathologists

CD14,EPR3653,7,Commercial product, extensive titration and validation in tonsils and tumor-free lymph nodes, reviewed by two independent board-certified hemato-pathologists

CD8,C8/144B,8,Custom conjugation of commercially available unconjugated antibody, extensive titration and validation in tonsils and tumor-free lymph nodes, reviewed by two independent board-certified hemato-pathologists

Kappa light chain,L1C1,70,Custom conjugation of commercially available unconjugated antibody, extensive titration and validation in tonsils and tumor-free lymph nodes, reviewed by two independent board-certified hemato-pathologists

CD45RA,HI100,21,Commercial product, extensive titration and validation in tonsils and tumor-free lymph nodes, reviewed by two independent board-certified hemato-pathologists

CD11b,EPR1344,28,Commercial product, extensive titration and validation in tonsils and tumor-free lymph nodes, reviewed by two independent board-certified hemato-pathologists

Granzyme B,EPR20129-217,81,Commercial product, extensive titration and validation in tonsils and tumor-free lymph nodes, reviewed by two independent board-certified hemato-pathologists

CD31,C31.3 + C31.7 + C31.10,51,Commercial product, extensive titration and validation in tonsils and tumor-free lymph nodes, reviewed by two independent board-certified hemato-pathologists

CD45,2B11+PD7/263,56,Commercial product, extensive titration and validation in tonsils and tumor-free lymph nodes, reviewed by two independent board-certified hemato-pathologists

CD38,EPR4106,3,Commercial product, extensive titration and validation in tonsils and tumor-free lymph nodes, reviewed by two independent board-certified hemato-pathologists
CD44,IM7,45,Commercial product, extensive titration and validation in tonsils and tumor-free lymph nodes, reviewed by two independent board-certified hemato-pathologists
CD15,MMA,14,Commercial product, extensive titration and validation in tonsils and tumor-free lymph nodes, reviewed by two independent board-certified hemato-pathologists
Lambda light chain,Lamb14,26,Custom conjugation of commercially available unconjugated antibody, extensive titration and validation in tonsils and tumor-free lymph nodes, reviewed by two independent board-certified hemato-pathologists
Mast cell tryptase,AA1,71,Commercial product, extensive titration and validation in tonsils and tumor-free lymph nodes, reviewed by two independent board-certified hemato-pathologists

Flow Cytometry

Plots

Confirm that:

- The axis labels state the marker and fluorochrome used (e.g. CD4-FITC).
- The axis scales are clearly visible. Include numbers along axes only for bottom left plot of group (a 'group' is an analysis of identical markers).
- All plots are contour plots with outliers or pseudocolor plots.
- A numerical value for number of cells or percentage (with statistics) is provided.

Methodology

Sample preparation

LN-derived cells were thawed, washed and stained for viability using a fixable viability dye e506 (Thermo Fisher Scientific) and for different surface markers depending on the experimental set-up. For subsequent intracellular staining, cells were fixed and permeabilized with the intracellular fixation/permeabilization buffer set (Thermo Fisher Scientific) and stained. Then, cells were analyzed.

Instrument

LSR Fortessa (BD Biosciences)

Software

FACSDiva (BD Biosciences, version 8), FlowJo (v10.8.0)

Cell population abundance

Not relevant. Sorting was not applied.

Gating strategy

Gating strategies are summarized in detail in Supplementary Figure 2 and 3.

- Tick this box to confirm that a figure exemplifying the gating strategy is provided in the Supplementary Information.